



Université de Bretagne Occidentale

MASTER DES SCIENCES DE LA MER ET DU LITTORAL  
*Université de Bretagne Occidentale*  
*Institut Universitaire Européen de la Mer*



Stage 2017–2018  
Charly de Marez  
M2 Marine Sciences

---

## Lee waves in the Gulf Stream

---

**Abstract :** The generation of lee waves in the path of the Gulf Stream is studied using a CROCO realistic simulation. The same signature of lee waves as in satellite observations is observed. In particular, a large amount of lee wave is generated where the Gulf Stream flows above the Charleston Bump. These waves are shown to match with the linear theory describing topographically-generated internal waves. The study of the energetic budget in the interior highlights that the nonlinearities of lee waves above the Charleston Bump account for about 1% of the dissipated energy by the lee waves in the global ocean.

**Key words :** *Internal waves, lee waves, topography, Gulf Stream.*

Advisors: **Jonathan GULA** and **Noé LAHAYE**

Contact: [gula@univ-brest.fr](mailto:gula@univ-brest.fr)

Laboratoire d'Océanographie Physique et Spatiale

*Rue Dumont d'Urville*

*29280 Plouzané*

<http://www.umr-lops.fr/>



August 30, 2018

## Remerciements

Avant de commencer la présentation du travail que j'ai effectué durant ce stage, je tiens à remercier l'ensemble des personnes avec qui j'ai échangé, partagé et appris.

Tout d'abord je remercie l'ensemble de l'équipe pédagogique du Master Marine Physics pour m'avoir fait découvrir l'océan sous un autre jour, à travers les nombreuses connaissances théoriques transmises tout au long de l'année. J'aimerais également remercier le personnel du LOPS pour son accueil pendant ces cinq mois.

En particulier, mes remerciements s'adressent à mes encadrants, M. Jonathan Gula et M. Noé Lahaye, pour le temps qu'ils m'ont accordé au cours duquel j'ai pu profiter de leur grande patience et de leur pédagogie. Les nombreux échanges que j'ai pu avoir avec eux m'ont permis d'avancer à mon rythme dès le début du stage et de ne jamais me sentir seul devant les différents obstacles rencontrés.

Je tiens également à remercier les différents doctorants et stagiaires du laboratoire avec lesquels j'ai pu échanger et qui ont su me donner de nombreux conseils avisés.

## Contents

<b>1</b>	<b>Introduction</b>	<b>2</b>
<b>2</b>	<b>Theoretical prediction of lee waves</b>	<b>5</b>
2.1	General considerations . . . . .	5
2.2	General dispersion relationship of linear internal waves . . . . .	5
2.3	Hydrostatic condition . . . . .	6
2.4	The case of lee waves . . . . .	6
2.5	Lee waves solutions . . . . .	7
2.5.1	Constant N and U . . . . .	8
2.5.2	Varying N and U . . . . .	9
2.6	Important other variables for the study of lee waves . . . . .	9
2.7	Numerical prediction of lee waves . . . . .	10
2.8	Rigid lid condition . . . . .	11
<b>3</b>	<b>The simulation</b>	<b>11</b>
3.1	Simulation outputs . . . . .	12
3.2	Comparison with satellite observations . . . . .	13
<b>4</b>	<b>Lee waves in the gulf stream</b>	<b>15</b>
4.1	Global evolution of lee waves and filtering process . . . . .	15
4.2	Comparison with 3D linear theory . . . . .	16
4.3	Diagnostics over the bump . . . . .	19
<b>5</b>	<b>Dissipation, mixing and non-linear processes</b>	<b>22</b>
5.1	Bottom mixed-layer depth from in-situ data . . . . .	22
5.2	Quantification of the dissipation and energy budget . . . . .	23
5.3	Focus on local dissipation . . . . .	25
<b>6</b>	<b>Conclusion</b>	<b>28</b>
<b>A</b>	<b>Basic theory for the ocean dynamics</b>	<b>29</b>
A.1	From momentum equations to primitive equations . . . . .	29
A.2	Density evolution and Brunt-Väisälä frequency . . . . .	29
<b>B</b>	<b>WKBJ approximation</b>	<b>29</b>
<b>C</b>	<b>Transect from gliders</b>	<b>30</b>
<b>D</b>	<b>Time evolution of dissipation</b>	<b>31</b>
<b>E</b>	<b>Hydraulic jump event</b>	<b>32</b>
<b>F</b>	<b>Energy conversion into lee waves</b>	<b>33</b>

## 1 Introduction

The ocean and the atmosphere form a coupled dynamic and thermodynamic system, principally forced by the incident solar radiation. Heat fluxes create large scale motions in the atmosphere and temperature gradients. Such atmospheric gradients create horizontal density variations in the ocean, which lead to pressure gradients and velocity field (i.e oceanic currents).

The ocean-atmosphere system is highly non-linear (Navier-Stokes equations and thermodynamics). The scales interact with each other and the spectrum of motions is continuous. One usually distinguishes four typical scales:

The planetary scale ( $L \geq 250$  km) with large currents forced by the wind (e.g. the Gulf Stream, the Kuroshio). At this scale the motions are dominated by the rotation and the stratification, and the dynamics can be described by the *geostrophic balance*<sup>1</sup>. The fluid moves principally horizontally. The input of energy by the wind in the whole ocean through such currents is estimated to be 1 TW [23]. The meso-scale ( $50 \text{ km} \leq L \leq 250 \text{ km}$ ) describes the vortices and the jets created by intensification or by instability of large scale currents. The submeso-scale ( $250 \text{ m} \leq L \leq 50 \text{ km}$ ) contains filaments and small vortices coming from the breaking or the interactions of larger scales (e.g. through instabilities). At this scale the rotation of earth becomes negligible. Finally, the fine scale contains essentially isotropic -3D- motions (up to the dissipation scales), because the stratification has no more impact on the dynamics.

Because of the stratification and the rotation, waves in the oceans can occur in the interior of the fluid. Such waves are called *internal waves*. Three types of internal wave occur in the ocean:

- Near-inertial waves which are primarily forced by the atmosphere (i.e the winds) with a frequency close to one day. This kind of waves represents about half the kinetic energy in the internal wave spectrum.
- Internal tides generated by the barotropic tide flowing over topographic features and are generated at the frequency of the tides. About 1.2 TW of energy is converted in such waves in the global deep ocean [15].
- Lee waves generated by currents (mostly geostrophic ones) flowing over rough topography. If the mean current is stationary, such waves are stationary, with a null frequency observed in a fixed frame of reference. It has been estimated that 0.2 TW is converted from geostrophic currents to internal lee waves [13]. This put forth the proposition that about 20% of the wind input in the ocean forces the generation of lee waves.

Generation of lee waves can be very strong when the near-bottom current is intense and the topography very rough. The understanding of these waves is a major issue in physical oceanography since they provide a mechanism for the transfer of energy from large-scale flows to turbulent length scales [5]. A lot of study focuses on lee waves occurring in the Drake Passage (e.g. [4], [14]) because the intense Antarctic Circumpolar Current (ACC) flows above large topographic features. For some years now, another region has been recognized being an important area for lee wave generation: the Gulf Stream region.

---

<sup>1</sup>Equilibrium between the rotation of earth and the horizontal pressure gradients

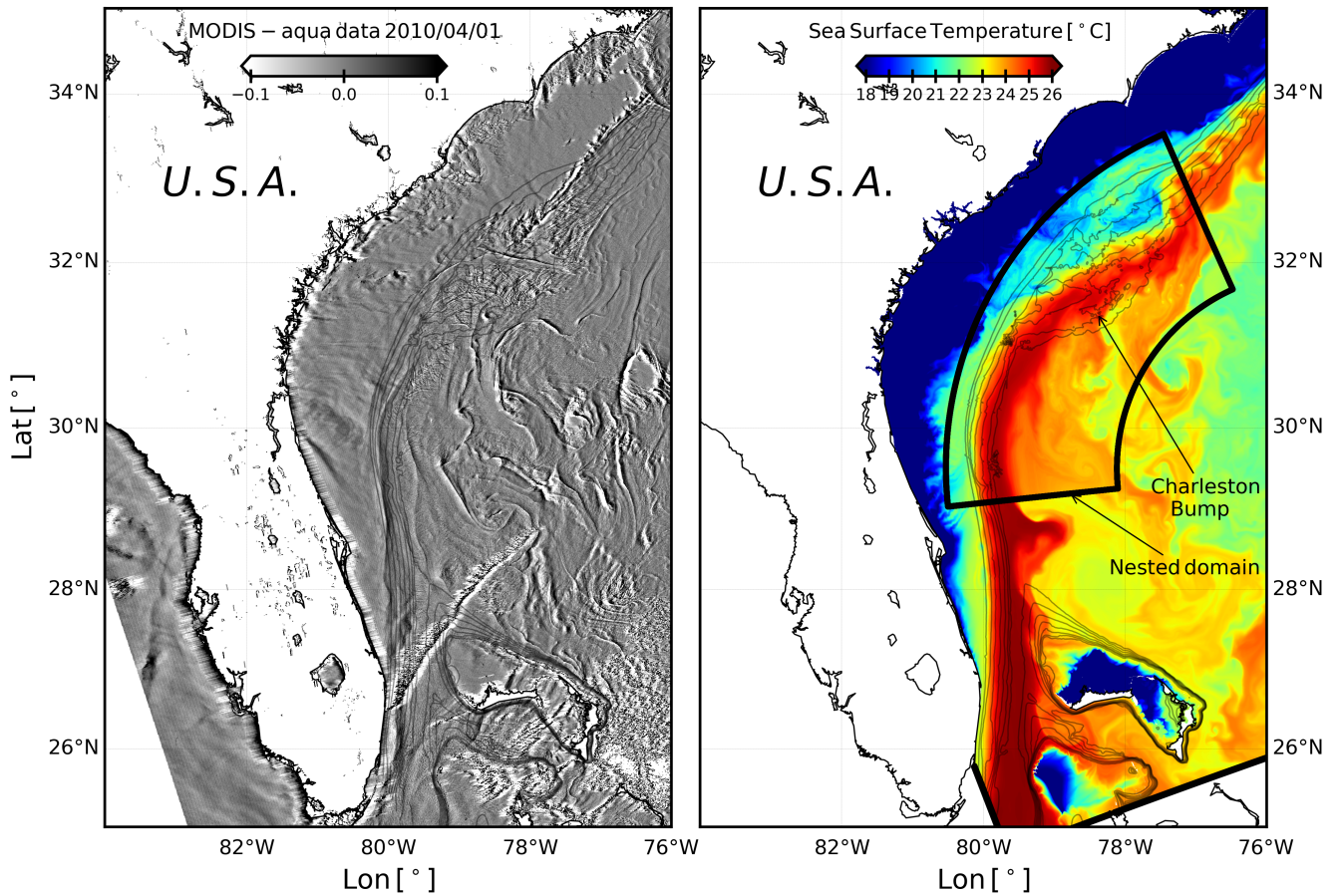


Figure 1: Observations in the Gulf Stream region. (left) Surface roughness from sun glitter satellite observation. (right) Sea surface temperature from CROCO simulation, the black curved area highlights the domain of the simulation discussed later. Gray contours indicate the bathymetry levels from 0 m to 800 m every 100 m.

In the North Atlantic, an anticyclonic gyre is forced by the wind at the scale of the basin. The western intensification<sup>2</sup> generates a northward and powerful current at the western boundary: the Gulf Stream. This current starts at the Strait of Florida and flows northward along the U.S. continental shelf before leaving the coast at Cape Hatteras. The sea surface temperature in the region of the Gulf Stream is shown in Fig. 1(right panel). An important along-shelf temperature gradient is visible, which is associated with the northward current through geostrophic balance. This current is very intense, flowing up to  $2 \text{ m s}^{-1}$  in some regions. Near  $31.5^\circ\text{N}, 79^\circ\text{W}$ , a prominent topographic feature is present off the coasts of South Carolina and Georgia: it is called the Charleston Bump. This feature is remarkable because it is located in the path of the Gulf Stream, and it creates an area of very shallow ( $O(500)$  m) and intense ( $O(1)$   $\text{m s}^{-1}$ ) flow. It has been shown that the Charleston Bump has a big influence on the shape of the Gulf Stream and that it exerts an important drag upon it [8].

Along the path of the Gulf Stream, by looking at sun glitter images, one can see the the signature of internal waves (Fig.1(left panel)) and particularly above the Charleston Bump. These signa-

<sup>2</sup>Phenomenon linked to the rotation of the earth which leads to the intensification of the currents at the western boundaries of the basins.

tures in satellite observations appear to be linked to bathymetric features and has been identified as lee waves surface signature [24]. Other studies using seagliders<sup>3</sup> have identified typical patterns of topographically-generated lee waves in this specific region [20]. Such observations of lee waves in the Gulf Stream have already been made a long time ago by observing the patchiness of seabird distribution at the surface [9].

The study of lee waves raise some important questions: (1) Under which conditions do the lee waves can be generated in the oceanic context ? (2) What are their properties (wavelength, frequency, energy flux...) ? (3) Can observed waves properties be understood using simple (e.g. linear) theoretical models ? (4) Are such waves able to generate some dissipation in the ocean, and what is their impact on the energetic budget in the ocean ?

The work I have done during this internship aims at characterizing the generation of lee waves in the wake of topographic seamounts along the Gulf Stream path using theoretical analysis and numerical simulations. This report presents the different tools and diagnostics implemented to study this phenomenon. The first section discusses theoretical aspects of the lee wave phenomenon. The second section presents the realistic simulation used to study the Gulf Stream region. Diagnostics and characterization of lee waves within the simulation are then discussed in the third section. Finally, the fourth section focuses on non-linear aspects of the lee wave phenomenon.

---

<sup>3</sup>Quasi-Lagrangian platforms carrying temperature and salinity sensors.

## 2 Theoretical prediction of lee waves

This section aims at presenting theoretically the lee wave phenomena. Starting from the main equations underlying physical oceanography, a short discussion is firstly made about internal waves. Secondly, a focus on the specific case of internal lee waves is made.

### 2.1 General considerations

For the study of oceanic fluid dynamics, two main parameters have to be considered: stratification (described by the vertical distribution of the density  $\rho$ ) and rotation. The ocean can be described by incompressible Navier-Stokes equation in a rotating frame, and an equation of state  $\rho = \rho(T, S, P)$ , with  $T$  the temperature,  $S$  the salinity and  $P$  the pressure. This problem being extremely complex, it can be simplified by considering some approximations [22] (details of the calculations are presented in appendix A). Far from the equator and assuming the Boussinesq approximation, the ocean can be described by a set of equation called *primitive equations*:

$$\frac{d}{dt} \mathbf{u} + f \mathbf{e}_z \times \mathbf{u} = -\frac{1}{\rho_0} \nabla P - \frac{\rho'}{\rho_0} g \cdot \mathbf{e}_z + \mathbf{F} + \mathbf{D} \quad (1)$$

where  $\mathbf{u} = (u, v, w)$  is the velocity of the fluid,  $\frac{d}{dt} = \partial_t + u \partial_x + v \partial_y + w \partial_z$  the material derivative,  $g = 9.81 \text{ m.s}^{-2}$  the gravity,  $f = 2\Omega \sin \phi$  the Coriolis parameters ( $\phi$  is the latitude),  $\mathbf{e}_z$  the normal vector of the local frame and  $\mathbf{F} + \mathbf{D}$  any term for forcing and dissipation (for instance wind forcing and Laplacian diffusion).

The density is decomposed into a constant component  $\rho_0$ , a mean stratification which varies along the z-axis (i.e the vertical axis)  $\bar{\rho}(z)$  and a anomaly which drives the dynamic in the fluid  $\rho'$ , such that:

$$\rho = \rho_0 + \bar{\rho}(z) + \rho'(t, x, y, z). \quad (2)$$

The equation describing the evolution of density is:

$$-\frac{g}{\rho_0} \frac{d}{dt} \rho' + w N^2 = 0. \quad (3)$$

$N$  is the Brunt-Väisälä frequency defined by

$$N^2 = -\frac{g}{\rho_0} \partial_z \rho. \quad (4)$$

This quantity controls the static stability of the fluid. On the one hand  $N^2 > 0$  implies that the density decreases with  $z$  (the fluid at the surface of the ocean is lighter than the one below). Thus, if a perturbation is introduced in the system the fluid particles will oscillate around an equilibrium position. On the other hand, if  $N^2 < 0$  the position of the fluid particles will diverge, and convection will occur.

### 2.2 General dispersion relationship of linear internal waves

By linearizing equations (1) and (3) around a rest state, and by considering incompressibility, one obtains the following system in a case without forcing and dissipation:

$$\left\{ \begin{array}{ll} \partial_t u - fv = -\frac{1}{\rho_0} \partial_x P & (a) \\ \partial_t v + fu = -\frac{1}{\rho_0} \partial_y P & (b) \\ \partial_t w + \frac{\rho'}{\rho_0} g = -\frac{1}{\rho_0} \partial_z P & (c) \\ -\frac{g}{\rho_0} \partial_t \rho' + w N^2 = 0 & (d) \\ \partial_x u + \partial_y v + \partial_z w = 0 & (e) \end{array} \right. \quad (5)$$

After some algebra, an equation for  $w$ , the vertical velocity within the fluid is obtained[1]:

$$\partial_{tt}(\Delta w) + f^2 \partial_{zz} w + N^2 \Delta_h w = 0. \quad (6)$$

where  $\Delta$  and  $\Delta_h$  are respectively the Laplacian and the horizontal Laplacian operators. Assuming there exists a monochromatic wave solution of equation (6) such that  $w = w_0 e^{i(kx+my+nz-\omega t)}$ , where  $\omega$  is the frequency of the wave, and  $\mathbf{k} = (k, m, n)$  its wavevector, one can derive the dispersion relationship of internal waves in a rotating and stratified fluid:

$$n^2 = (k^2 + m^2) \left( \frac{N^2 - \omega^2}{\omega^2 - f^2} \right). \quad (7)$$

### 2.3 Hydrostatic condition

In some cases, it can be interesting to consider the hydrostatic approximation in order to simplify the equations. To do so, the term  $\frac{\rho'}{\rho_0} g$  has to be much greater than  $\partial_t w$  in equation (5)(c). Combining equations (5)(c) and (5)(d) and giving a time scale  $T \sim \omega^{-1}$ , a criterion for the validity of hydrostatic hypothesis is obtained:

$$\frac{\omega}{N} \ll 1 \rightarrow \text{Hydrostatic} \quad (8)$$

### 2.4 The case of lee waves

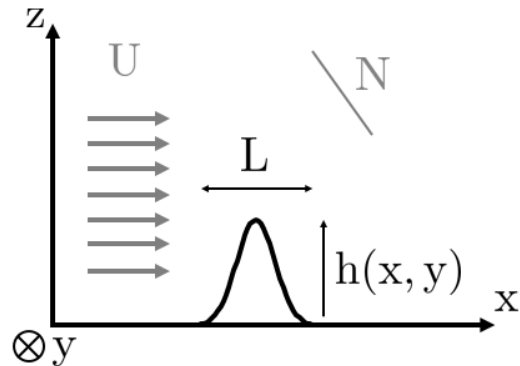


Figure 2: Lee wave situation: a fluid with stratification  $N$  flows with a horizontal velocity  $U$  over a topography of shape  $h(x, y)$  which typical horizontal scale is  $L$ .

When the mean current encounters a bottom topography, a vertical displacement of fluid particles is forced. Because of the stratification, this forcing induces the propagation of waves within the fluid. That kind of wave is called *lee waves*. This part presents some elements required to understand the theory of such waves.

Consider a steady background flow  $\mathbf{U} = (U, 0, 0)$  along the  $x$ -axis and a stratification  $N$  over a topography  $h(x, y)$  of typical length  $L$  as presented in Fig. 2. In the presence of the mean flow, a Doppler-shifted frequency  $\omega_a = \omega + \mathbf{k} \cdot \mathbf{U}$  would be measured by a stationary observer. Therefore, in the frame of the current the frequency is imposed by the current such that  $\omega = -kU$ . If it's periodic, the topography also imposes the along-flow horizontal wavenumber  $k \sim 1/L$  (as we will see in the following). Considering the dispersion relation (7), internal waves can only propagate if  $n \in \mathbb{R}$ . For the case of lee waves, it results in the propagation condition:

$$|f|/|U| < k < |N|/|U|. \quad (9)$$

In the case studied in this report, one can assume a typical stratification  $N \sim 10^{-2} \text{ s}^{-1}$ , a barotropic (i.e homogeneous with respect to vertical) flow  $U \sim 1 \text{ m/s}$ , a typical size of seamounts  $L \sim 1 \text{ km}$  and a coriolis parameter  $f \sim 10^{-4} \text{ s}^{-1}$ . Therefore, in first approximation and to keep the calculations tractable, the contribution of rotation in (7) is neglected.

Finally the two dispersion relations for hydrostatic and non hydrostatic lee waves are:

$$\begin{cases} n^2(k, m) = k^{-2}(k^2 + m^2) \left( \frac{N^2}{U^2} - k^2 \right) & \text{for non-hydrostatic lee waves (a)} \\ n^2(k, m) = k^{-2}(k^2 + m^2) \frac{N^2}{U^2} & \text{for hydrostatic lee waves (b)} \end{cases} \quad (10)$$

In the following of this section we will keep both hydrostatic and non-hydrostatic dispersion relations to be complete, knowing that in the second part of this report we will only consider the hydrostatic solution.

## 2.5 Lee waves solutions

Knowing the wave form of the internal waves and neglecting rotation, equation (6) can be re-written as:

$$\partial_{xx}(\Delta w) + \frac{N^2}{U^2}(\Delta_h w) = 0. \quad (11)$$

Assuming a radiation condition at the top of the domain, and the condition that the flow follows the topography at the bottom, such that:

$$\begin{cases} w \neq 0 & \text{at the top (a)} \\ w = U(z=0) \partial_x h(x, y) & \text{at the bottom (b)} \end{cases} \quad (12)$$

and defining the vertical displacement of a streamline  $\eta$  such that  $w = U \partial_x \eta$ , the bottom boundary condition becomes:

$$\eta(x, y, z=0) = h(x, y), \quad (13)$$

which means that the bottom of the domain is equal to a streamline.

The solution of the problem defined by (11) and (13) may be obtained by using a 2D Fourier transform over the  $(x, y)$  plane. The 2D Fourier transform is defined by:

$$\tilde{\eta}(k, m, z) = \int_{-\infty}^{+\infty} \int_{-\infty}^{+\infty} \eta(x, y, z) e^{i(kx+my)} dx dy. \quad (14)$$

In Fourier space, the problem becomes:

$$\begin{cases} \partial_{zz}\tilde{\eta}(k, m, z) + n^2\tilde{\eta}(k, m, z) = 0 \\ \tilde{\eta}(k, m, z = 0) = \tilde{h}(k, m) \end{cases} \quad (15)$$

where  $\tilde{h}(k, m)$  is the Fourier transform of the topography of general shape  $h(x, y)$ . Finally, the solution of the problem is obtained by calculating the inverse Fourier transform :

$$\eta(x, y, z) = \frac{1}{4\pi^2} \int_{-\infty}^{+\infty} \int_{-\infty}^{+\infty} \tilde{\eta}(k, m, z) e^{i(kx+my)} dk dm \quad (16)$$

### 2.5.1 Constant N and U

Assuming a constant stratification  $N$  and a constant velocity along the  $x$ -axis  $U$ , the solution of the problem (15) with an upper radiation condition is

$$\tilde{\eta}(k, m, z) = \tilde{h}(k, m) e^{i n(k, m) z}, \quad (17)$$

and thus

$$\eta(x, y, z) = \frac{1}{4\pi^2} \int_{-\infty}^{+\infty} \int_{-\infty}^{+\infty} \tilde{h}(k, m) e^{i(kx+my+n(k,m)z)} dk dm \quad (18)$$

where  $n(k, m)$  is determined with relations (10) (taking the positive square root of  $n^2$  which implies a positive group velocity).

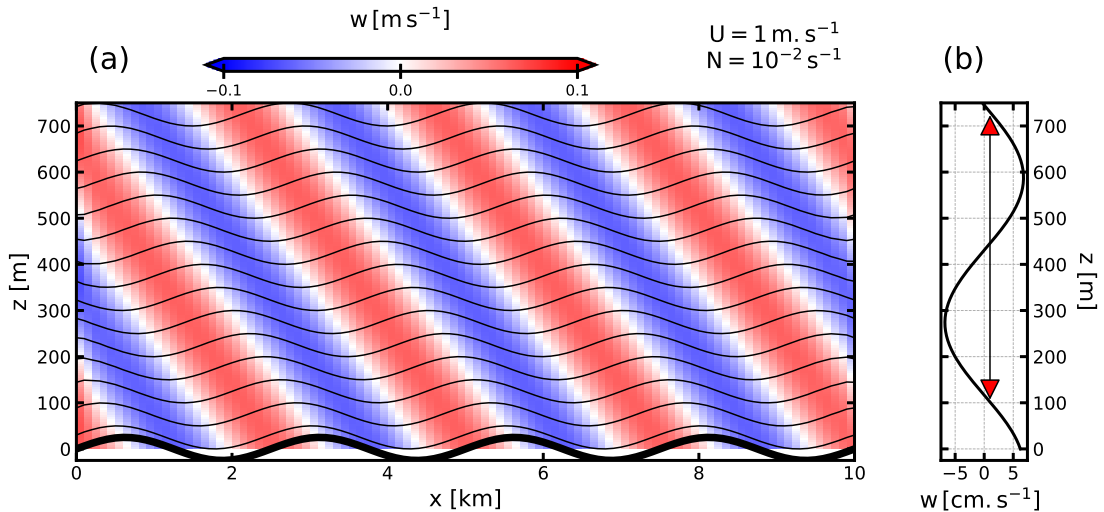


Figure 3: Lee wave hydrostatic solution computed numerically from equation (18) with  $U = 1 \text{ ms}^{-1}$  and  $N = 1.10^2 \text{ s}^{-1}$ . (a) Vertical velocity from calculation in the  $(x, z)$  plane (side view), solid lines are the streamlines  $\eta$ . The bold line represents the shape of the bathymetry  $h(x)$  used in the calculation. (b) Vertical velocity from calculation at  $(x, y) = (10, 0) \text{ km}$ , double arrow indicates the vertical theoretical wavelength for 2D hydrostatic flow ( $U/N$ ).

The most common example of solution is the 2D, sinusoidal topography such as

$$h(x) = h_0 \cos(k_T x), \quad (19)$$

where  $k_T$  is the wavenumber of the topography. The Fourier transform of  $h(x)$  is simply  $\tilde{h}(k) = \delta(k_T - k)$ . Therefore, the integral (18) collapses to a simply horizontal periodic solution with a wavenumber  $k_T$ . In the presence of a periodic topography, an internal wave is generated, which wavenumber is imposed by the topography such as :

$$\eta(x, z) = h_0 \cos(k_T x + n z) \quad (20)$$

where  $n$  is equal to  $N/U$  in the 2D hydrostatic case .

The numerical computation of equation (18) for a shape of topography defined with (19) is presented in Fig. 3. The horizontal wavelength of the field corresponds to the wavelength imposed by the topography. Furthermore, the vertical wavelength is found equal to  $U/N$  as predicted by the theory.

### 2.5.2 Varying N and U

We assume that the stratification and the x-axis velocity are varying with depth as  $N(z)$  and  $U(z)$ . Firstly the dispersion relation (10) has to be modified by taking into account the shear of the flow [1]:

$$\begin{cases} n^2(k, m, z) = k^{-2}(k^2 + m^2) \left( \frac{N(z)^2}{U(z)^2} + \frac{U_{zz}(z)}{U(z)} - k^2 \right) & \text{for non hydrostatic lee waves (a)} \\ n^2(k, m, z)^2 = k^{-2}(k^2 + m^2) \left( \frac{N(z)^2}{U(z)^2} + \frac{U_{zz}(z)}{U(z)} \right) & \text{for hydrostatic lee waves (b)} \end{cases} \quad (21)$$

Because  $n^2$  varies with depth, the solution of (15) is not as simple as (17). One way to compute the solution is to use the WKBJ approximation [6] (see appendix B). The solution of (15) becomes

$$\tilde{\eta}(k, m, z) = \tilde{h}(k, m) \sqrt{\frac{n(0)}{n(z)}} \exp\left(i \int_0^z n(k, m, z) dz\right), \quad (22)$$

### 2.6 Important other variables for the study of lee waves

Solving problem (15) and going back into physical space gives the displacement of the streamlines  $\eta(x, y, z)$ . The vertical velocity field is obtained using its definition  $w = U \partial_x \eta$ . In the ocean, the movement of fluid being principally horizontal, the vertical velocity can be considered in first approximation as a perturbation, such as  $w \sim w'$ , where the ' denotes the lee wave induced perturbation. The measure of vertical velocity will thus be the principal way to observe and characterize lee waves in the numerical model.

To go further, some other variables have to be calculated, in particular, the pressure anomaly  $p'$ . To do so, assuming that the displacement of a streamline creates an anomaly of density and using hydrostatics, the variation of pressure anomaly in the water column is obtained with:

$$\partial_z p' = -\eta \rho_0 N^2. \quad (23)$$

The pressure anomaly at a given depth is thus

$$p'(z) = p'(z=0) - \int_0^z dz \eta \rho_0 N^2. \quad (24)$$

Because of the upper radiation condition,  $p'(z \rightarrow +\infty) \rightarrow 0$ , the integration of equation (23) between  $z = 0$  and  $z = +\infty$  gives :

$$p'(z=0) = \frac{\rho_0}{4\pi^2} \iint_{-\infty}^{+\infty} dk dm \tilde{h}(k, m) \frac{e^{i(kx+my)}}{i n(k, m)}. \quad (25)$$

We compute horizontal velocity anomalies ( $u'$ ,  $v'$ ) associated with this pressure anomaly. Assuming that the mean current  $U$  is still along the  $x$ -axis, the linearized equations of movement are:

$$\begin{cases} U\partial_x u' = -\left(\frac{1}{\rho_0}\partial_x p' + (\partial_z U)w'\right) \\ U\partial_x v' = -\frac{1}{\rho_0}\partial_y p' \end{cases} \quad (26)$$

## 2.7 Numerical prediction of lee waves

To predict the shape of lee waves in different cases, I implemented a code which allows to compute the 3D, linear and hydrostatic theoretical prediction of lee wave generation for a given topography and a given profile of mean current  $U(z)$  and stratification  $N(z)$ . The shape of the topography and the profiles can be analytical like the results presented in Fig. 3 and 4 or arbitrary, like in Fig. 8, 9 and 10 where the topography and the profiles are from the CROCO simulation that will be discussed later. In each case, the mean current is along the  $x$ -axis, and  $U$  and  $N$  are independent of the horizontal position.

The code computes the Fourier transform of  $\eta$  from equation (22). To avoid problems at the edge of the domain, a Han window is applied on the topography before the calculation of  $\tilde{h}(k, m)$ . The physical field is obtained by going back into physical space.

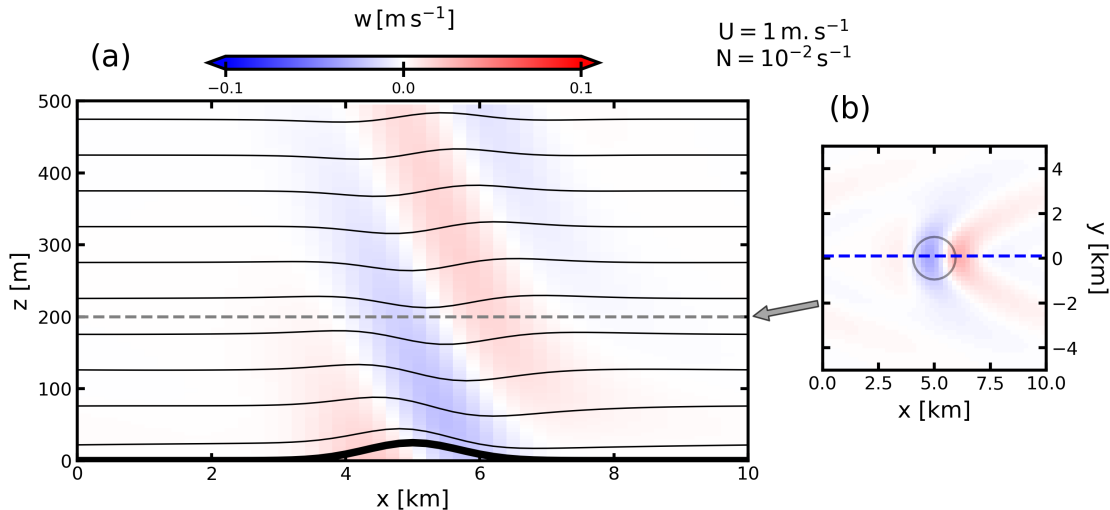


Figure 4: Lee wave hydrostatic solution computed numerically from equation (18) with  $U = 1 \text{ ms}^{-1}$  and  $N = 1.10^2 \text{ s}^{-1}$ . (a) Vertical velocity from calculation in the  $(x, z)$  plane (side view), solid lines are the streamlines  $\eta$ . The bold line represents the shape of the bathymetry  $h(x, y)$  used in the calculation. The dashed gray line denotes the position of the horizontal section presented on the (b) panel. (b) Vertical velocity at  $z = 200 \text{ m}$ . The dashed blue line denotes the position of the section presented on the (a) panel. Grey contour in (b) indicates the bathymetry level at 10 m from the ground (i.e the position of the seamount).

A typical example of lee wave generation is when the mean current encounters an isolated seamount. The prediction of such an event is presented in Fig. 4. The result is quite similar in the  $(x, z)$  plane than the one for a cosinus topography (Fig. 3) with much less amplitude for vertical velocity. The numerical calculation allows us to represent such a solution while it can not be calculated analytically. Especially,

the production of vertical motion at the bottom can be understood easily with this example: when fluid particles are pushed toward the seamount by the mean current (between  $x \sim 4$  km and  $x \sim 5$  km) they climb over it and a positive vertical velocity is created which radiates upward. The same mechanism creates a negative vertical velocity behind the seamount (from  $x \sim 5$  km to  $x \sim 6$  km).

Finally, the 3 dimensionality of the calculation allows to predict the shape of the wave in the (x,y) plane. This prediction is important because large scale observations (especially satellite observations) of waves are made at the surface. Therefore it is the horizontal shape of waves which has to be characterized.

## 2.8 Rigid lid condition

The description of lee wave made previously is heavily dependent on the upper radiation condition imposed (12). In some cases a rigid lid condition is more adapted to the description of lee waves such that:

$$\begin{cases} w = 0 & \text{at the top (a)} \\ w = U(z=0) \partial_x h(x, y) & \text{at the bottom (b)} \end{cases} \quad (27)$$

It is all the more important when the vertical wavelength (imposed by the topography and the mean current) matches with the layer thickness. In such cases, a vertical modal structure of the wave is generated by reflection at the top. The theoretical and numerical resolution of the rigid lid problem is not as straightforward as the radiation problem. For non-varying  $U$  and  $N$ , the form of  $\eta$  is:

$$\eta(x, y, z) = \frac{1}{4\pi^2} \int_{-\infty}^{+\infty} \int_{-\infty}^{+\infty} \tilde{h}(k, m) \left( M e^{-i n z} + (1 - M) e^{i n z} \right) e^{i(kx+my)} dk dm, \quad (28)$$

with

$$M = \frac{e^{i n D}}{2i \sin(nD)}.$$

where  $D$  is the depth of the fluid. The presence of  $M$  thus allows the propagation of lee waves only when the modes interfere constructively. However, the denominator causes the integral to diverge for  $n = j \frac{\pi}{D}$  where  $j$  is an integer. The computation can be done by considering the Cauchy theorem for complex analysis.

An attempt of resolution has been done to add this condition in the theoretical code, but at this stage of the study, we are only able to predict the comportment of lee wave in the upper radiation condition.

In the following of this report, I present the different diagnostics and methods I implemented to observe the phenomenon of lee waves in the path of the Gulf Stream.

## 3 The simulation

In order to study the generation of lee waves in the Gulf Stream, a realistic simulation in the Gulf Stream region (around the Charleston Bump) is realized with the Coastal and Regional Ocean Community model (CROCO; previously called ROMS [17]). This model is widely used in the physical oceanography community. It solves the hydrostatic primitive equations (1) for the velocity  $\mathbf{u}$ , the temperature  $T$  and the salinity  $S$ , using a full equation of state for seawater [18]. Because the study focuses on very fine scales, a nesting approach is used. A parent simulation with coarser resolution is used to force the edges of a higher resolution simulation. The parent thus supplies the initial and boundary conditions for the nest. The successive horizontal grid resolutions are  $\Delta x \sim 750$  m for the parent, and  $\Delta x \sim 300$  m

for the nested domain. The two domains are presented in Fig. 1. The simulation has 128  $\sigma$ -levels (i.e. 128 vertical levels). This type of vertical discretisation allows levels to follow the topography, and thus avoids problems of advection and gradients at the bottom boundaries. The nested domain is chosen to be along the continental shelf, and it is centered around the Charleston Bump (see Fig. 1). The lateral edges of the domain are chosen far enough from the temperature front of the Gulf stream (i.e. the area of maximum velocity) in order to avoid advection problems at the edges of the domain.

The bathymetry is constructed from the SRTM30\_PLUS dataset. A gaussian smoothing kernel is used to avoid aliasing due to scales smaller than the resolution scale of the model. Simulations are forced with a monthly varying wind, and no tides were added. These three choices are important because they imply weak generation for some types of internal waves: no internal tides and a very few near-inertial waves.

The subject of the stage was not the construction of the model configuration, and a very little amount of time was used on numerical aspects. This allowed me to focus on physics questions. To further understand the parent simulation, and numerical aspect, see [8]. In the following "the simulation" refers to the simulation in the nested domain.

### 3.1 Simulation outputs

The simulations takes place in spring, and is about one month long from March 20th 2016 to April 12th 2016 with an output every hour. Throughout the simulation, the Gulf Stream flows into the domain through the southern boundary, follows the continental shelf, and flows out the domain through the northern boundary.

Snapshots of surface velocity are presented in Fig. 5. The horizontal velocity is important, up to  $2 \text{ m s}^{-1}$ . While it flows above the Charleston Bump, the Gulf Stream direction deflects and creates a quasi-stationary cyclonic eddy referred to as the Charleston Gyre [12]. Surface relative vorticity is presented in Fig. 5. It highlights the cyclonic structure above the Charleston Bump through positive vorticity patches.

The Eastern boundary of the simulation presents a large amount of submesoscale structures (i.e. of size  $< 30 \text{ km}$ , the Rossby deformation radius). Spring is a season favorable to the presence of such structures [3] because of the presence of a deep winter mixed layer at the surface of the ocean.

To allow the reader to visualize the movement of the fluid in the simulation, a video is available online at [this url<sup>4</sup>](https://www.youtube.com/watch?v=rBI3Tv5YXf0&feature=youtu.be), or by scanning the QR code supplied here.



<sup>4</sup><https://www.youtube.com/watch?v=rBI3Tv5YXf0&feature=youtu.be>

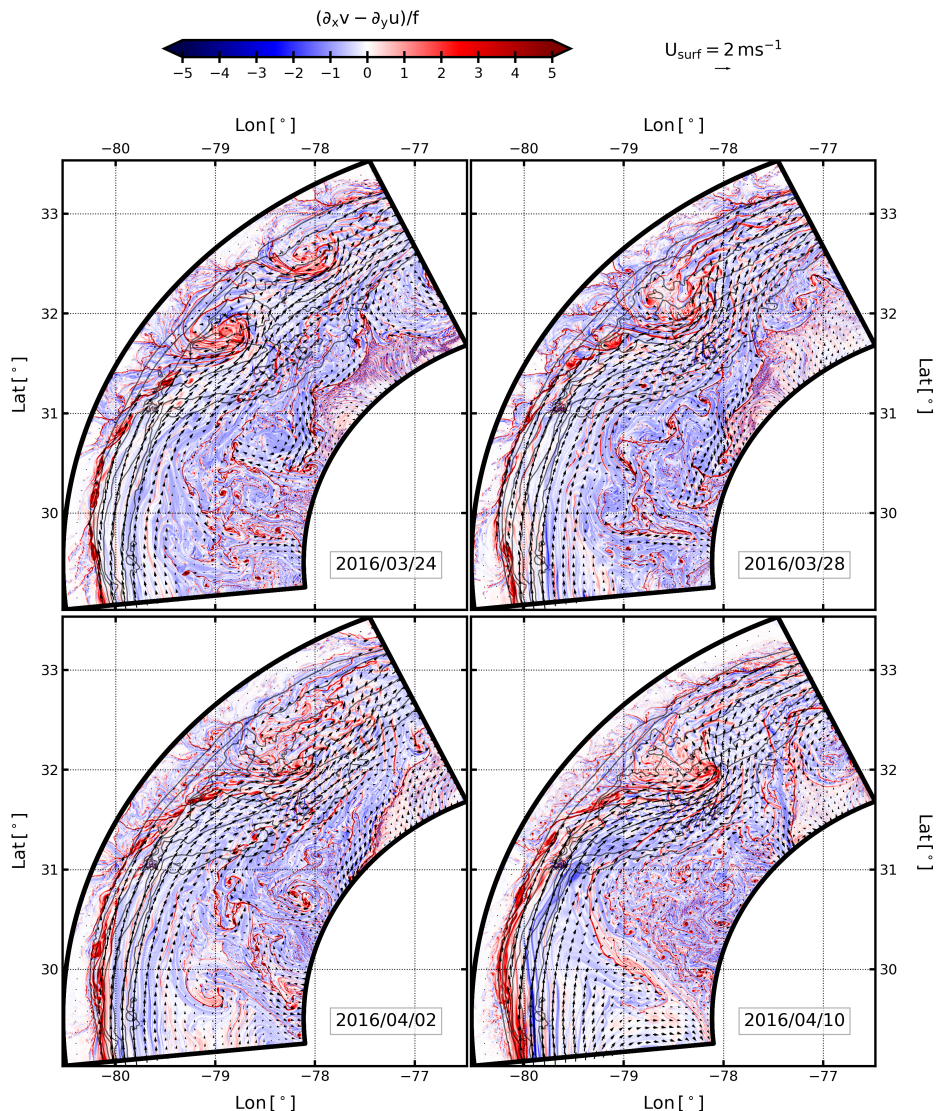


Figure 5: Snapshots of surface relative vorticity normalized by the Coriolis frequency at different times of the simulation. Gray contours represent the shape of local bathymetry (bathymetry levels at 200, 400 and 600 m), black arrows present the surface velocity field.

Section 2 put forth the proposition that when a mean current flows above a topography, it generates stationary waves propagating upward. In the simulation presented here, the powerful Gulf stream flows at  $O(1) \text{ m s}^{-1}$  above the Charleston Bump. This topography is rough and the fluid layer above is  $O(500) \text{ m}$  depth, which is quite shallow compared to the  $4000 \text{ m}$  mean depth of the global ocean. The condition are thus in place to allow the forcing and the propagation of internal lee waves.

### 3.2 Comparison with satellite observations

In this region, such waves have already been observed with SAR (Synthetic Aperture Radar) images taken by satellites passing over the Gulf Stream [24]. Another way to observe internal waves with satellite is by measuring the sun glint on the ocean surface with optical spectroradiometers. Fig. 6(a)

presents an image obtained on April 1st 2010 from radiance measured by the Moderate Resolution Imaging Spectroradiometer (MODIS) onboard the Terra satellite. The data has been high-passed at 25 km and has a resolution of 250 m. It shows the ocean surface roughness in the region of the Charleston Bump. Because divergent currents exhibit surface roughness signature [16], this kind of data provide observations of oceanic phenomena at scales  $O(1 - 10)$  km such as internal waves. Wavefront-like structures in the roughness observation (Fig. 6(a)) thus allow to qualitatively conclude on the presence of internal waves generated over the Charleston Bump in the path of the Gulf Stream.

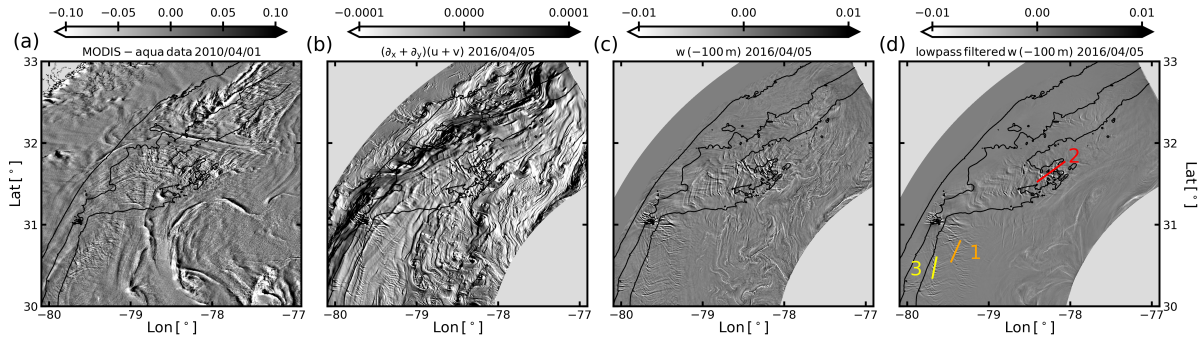


Figure 6: (a) Surface roughness from radiance measured with MODIS instrument onboard Aqua satellite on April 1st 2010, black solid contours are bathymetry levels for 200, 400 and 600m. (b) Snapshot of  $(\partial_x + \partial_y)(u + v)$  at the surface, from the CROCO simulation. (c) Snapshot of vertical velocity  $w$  at 100m depth, from the CROCO simulation. (d) Snapshot of lowpass filtered ( $T_{cut} = 4$  days) vertical velocity  $w$  at 100m depth, from the CROCO simulation ; yellow, orange and red lines denotes the location of sections discussed further. (b), (c) and (d) are taken at the same instant, on April 5th 2016

To compare these observations with the simulation, the term

$$(\partial_x + \partial_y)(u + v)$$

at the surface is shown in Fig. 6(b). Indeed, it has been proposed that surface roughness can be interpreted as a linear combination of the horizontal partial derivatives of horizontal velocities [16] such as

$$\text{roughness} \sim \alpha \partial_x u + \beta \partial_y u + \gamma \partial_x v + \delta \partial_y v.$$

The coefficients  $\alpha$ ,  $\beta$ ,  $\gamma$  and  $\delta$  are functions of (1) the wind direction and (2) the position of the measuring device with respect to the position of the sun. Setting these coefficients to 1 allows to have a first assumption of what could be the surface roughness in the simulation. Mesoscale and submesoscale turbulence within the simulation are very present in Fig. 6(b), notably because of shearing and divergent processes. Despite this, wavefront-like structures can be seen near  $31.5^\circ$  N,  $79^\circ$  W (on the Charleston Bump) or near  $30.5^\circ$  N,  $79.5^\circ$  W. Therefore, qualitatively, the same kind of internal waves that the ones observed by satellite appear in the simulation.

Conceptually, the easier way to understand the generation of internal (in particular lee) waves is to compute the vertical velocity within the fluid. We have seen that a seamount in the wake of a mean current create lee waves with horizontal patterns depending on different parameters (see Fig. 4(b)). The vertical velocity of the fluid at 100 m depth is shown on Fig. 6(c), at the same location and date than Fig. 6(b). The vertical velocity highlights the wavefront-like structures near the Charleston Bump discussed above. It also shows that these patterns are not only present at the surface but also below the thermocline (which is about  $O(50)$  m depth). A low-pass butterworth filter is applied on the simulation

outputs in order to extract quasi-stationary process within the simulation. The result is shown in Fig. 6(d). The cutting period has been chosen at 4 days to keep the variations of the current ( $O(1)$  week), and to remove all  $O(< 1)$  days processes. The low-passed field allows us to remove the rapidly-moving turbulent component of the velocity field. It highlights the fact that the wavefront-like structures observed near the Charleston Bump are quasi-stationary.

At this step of the study, quasi-stationary wave-like structures are seen in the simulation and seem to be in accordance with satellite observations of internal lee waves. The following part of this report aims at characterizing them and comparing them to the theoretical solutions of linear lee waves.

## 4 Lee waves in the gulf stream

### 4.1 Global evolution of lee waves and filtering process

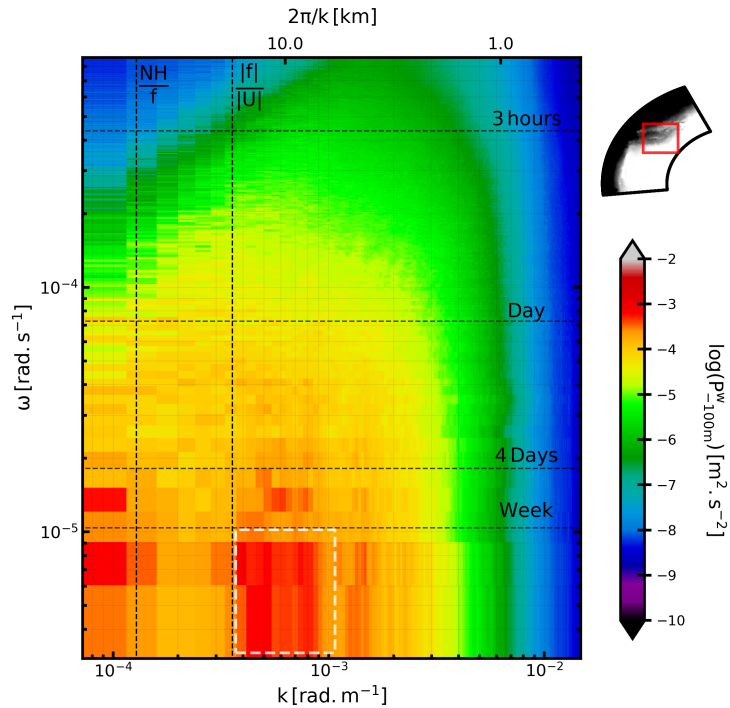


Figure 7:  $(k, \omega)$  power spectrum of vertical velocity at 100 m depth computed in the location presented on the top right panel. The white dashed rectangle highlights the temporal and spatial scales of the lee waves.

In the simulation, the Gulf Stream is quasi-stationary, and flows over a rough topography (including the Charleston Bump) as illustrated in Fig. 5. The variability of the Gulf stream is at a time scale of  $O(1)$  week. Because of the smoothing of the topography, typical size of seamounts is  $O(1 - 10)$  km. This situation is compatible with the generation of quasi-stationary lee waves of horizontal wavelength  $O(1 - 10)$  km. A  $(k, \omega)$  spectrum (dispersion diagram) of vertical velocity variance at 100 m depth ( $w_{100}(t, x, y)$ ) is calculated to visualize the temporal and spatial scales of processes (Fig. 7). This spectrum is computed over a squared area over the bump (see top right panel of Fig. 7).

To compute the spectrum, the spatial 2D Fast Fourier Transform (FFT) of  $w_{100}(t, x, y)$  is calculated, which gives a real and an imaginary part  $\hat{w}^r(t, k, l)$  and  $\hat{w}^i(t, k, l)$  where  $k$  and  $l$  are the horizontal wave numbers for axis  $x$  and  $y$ . The temporal 1D FFT of  $\hat{w}^r(t, k, l)$  and  $\hat{w}^i(t, k, l)$  is then calculated. It gives two complex fields  $\tilde{w}^r(\omega, k, l)$  and  $\tilde{w}^i(\omega, k, l)$ . To obtain the power spectral density, this quantities are recombined such as:

$$P_{-100m}^w(\omega, k, l) = \left| \frac{1}{4} \left( \tilde{w}^r \overline{\tilde{w}^r} + \tilde{w}^i \overline{\tilde{w}^i} \right) + \frac{1}{8} \left( \mathcal{R}(\tilde{w}^i) \mathcal{I}(\tilde{w}^r) - \mathcal{R}(\tilde{w}^r) \mathcal{I}(\tilde{w}^i) \right) \right|$$

where  $\bar{a}$  is the complex conjugate of  $a$ , and  $\mathcal{R}$  and  $\mathcal{I}$  are the complex and imaginary parts. Finally an azimuthal average is computed in the  $(k, l)$  space to keep only the norm of the spatial wavenumber.

An energetic region in the  $(k, \omega)$  space is present for spatial scales of  $O(10)$  km and temporal scales of  $O(> 1)$  weeks (dashed white rectangle in Fig. 7) which are the expected scales for lee waves. As seen in (9), internal waves can only propagate if  $|f|/|U| < k < |N|/|U|$ . This value here clearly limits the energetic region discussed earlier. This confirms that lee waves are visible in the energetic spectrum of vertical velocity. Here the value of  $|f|/|U|$  is calculated with a spatial average of the velocity at the bottom on April 5st 2016 (which is a day of important lee wave generations). Therefore, lee waves seem to be a preponderant process occurring over the Charleston Bump.

The spectrum also highlights the fact that lee waves have a temporal scale lower than 4 days and it confirms the accuracy of the low-pass filter used (presented in Fig. 6). In the following, most of the quantities showed are low-passed to isolate the lee wave signature.

## 4.2 Comparison with 3D linear theory

The theoretical code presented in section 2.7 is used to compare lee wave in the simulation with theory discussed in section 2.

Section 1 in Fig. 6 is an area where some isolated lee waves occur on April 5st 2016 above a relatively simple topography. This region is deeper than the Charleston Bump area, it allows to make the assumption of radiation condition (used in the theoretical code). Section 1 has been chosen to be mostly tangential to the mean current. A region of quasi-constant direction of the mean current is then chosen around the section. Mean vertical profile of velocity and stratification in the region are computed from simulation outputs (at a chosen time). They are smoothed by a Gaussian filter to avoid discontinuities and problems in the calculation of  $U_{zz}(z)$ . The topography is de-trended by removing a smoothed topography to keep only anomalies of topography (i.e. the seamounts). A Han window is applied on the de-trended topography. The theoretical prediction is presented in Fig. 8. It shows a horizontal cut of vertical velocity at 500 m depth. The comparison is made in Fig. 8 with an horizontal cut at 500 m depth of low-passed vertical velocity from the simulation in the region where profiles and topography have been extracted.

The signal of vertical velocity in the simulation at the edges of the domain is not consistent with what is calculated in the theoretical prediction. This is due (1) to the windowing which reduces intensity of the waves in the theoretical calculation and (2) to the impact of lee wave propagating from outside the domain (in the simulation). Despite this, the seamount at  $(x, y) \sim (5, 6)$  km generates a wave of shape and intensity very similar to the theoretical predictions. This kind of internal wave produces vertical velocity of  $O(1) \text{ cm s}^{-1}$ . It is quite intense in comparison with the -mostly horizontal-motions occurring in the ocean, and having vertical velocities of  $O(1) \text{ m days}^{-1}$ .

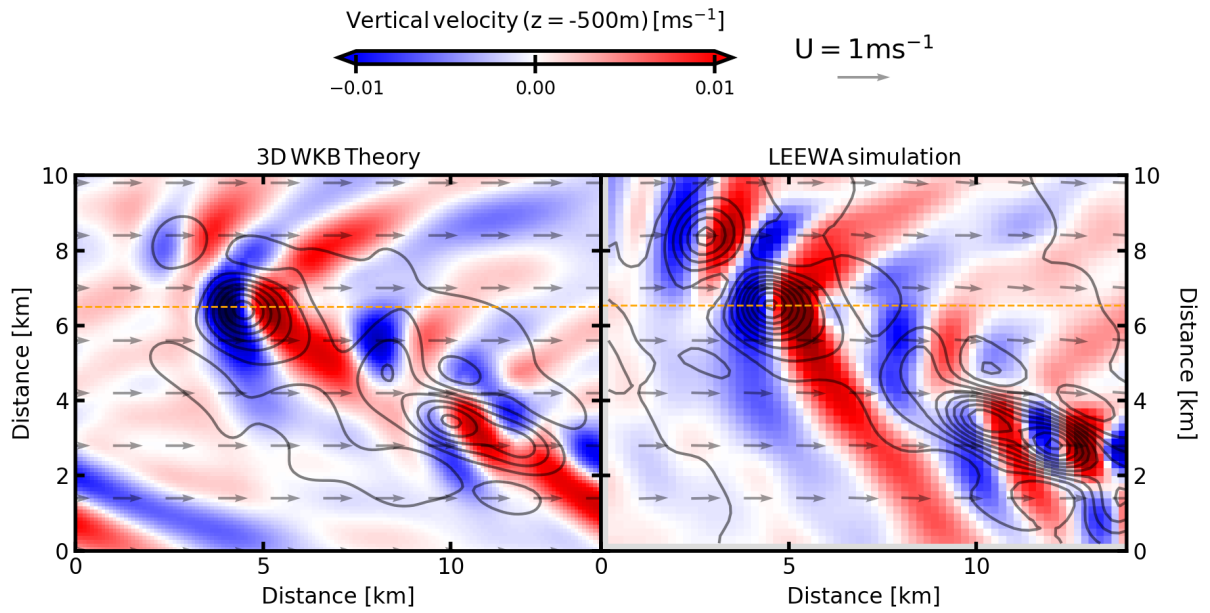


Figure 8: Vertical velocity at 500 m depth (horizontal cut) using 3D hydrostatic linear theory in the WKBJ approximation (left), and snapshot of time low-passed vertical velocity at the same depth from the CROCO simulation (right). The theoretical computation is processed with z-varying  $U$  and  $N$  profiles from the simulation (profiles are presented on Fig. 9), and with the topography of the domain considered. The orange dashed line is the location of section presented in Fig. 9, which is location 1 in Fig. 6

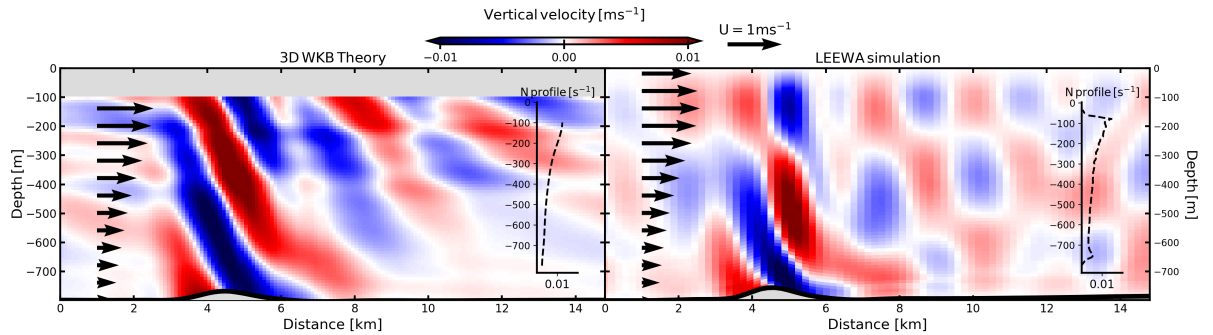


Figure 9: Vertical velocity at section 1 (indicated by the orange dashed line in Fig. 8 and Fig. 6), using 3D hydrostatic linear theory in the WKBJ approximation with radiation condition at the top (left), and snapshot of time low-passed vertical velocity at the same position from the CROCO simulation (right). Arrows indicate the velocity profile used for the calculation (left) and averaged over the section (right), inserts present profiles of stratification  $N$ . The topography is indicated by the bold line.

Vertical sections of vertical velocities for the theory and the simulation are shown in Fig. 9. The location of the section is indicated in Fig. 6 (section 1) and Fig. 9 (orange dashed line). These sections focus on the vertical structure of lee waves generated by the seamount at  $(x, y) \sim (5, 6)$  km in Fig. 8.

The global shape of the generated wave in the simulation matches with the theoretical prediction. In particular the ray inclination are the same. However, the patterns at the top of the domain are

clearly different. The generation of waves in the simulation seems to be very impacted by the rigid lid condition which is imposed by the surface of the fluid. As seen in part 2.8 rigid lid condition imposes the creation of vertical modes. From the surface to 400 m depth this modal structure is visible. Despite this, the bottom of the domain shows good agreement with the "radiating" linear solution. This distinction may be due to the fact that the energy which propagates downward after being reflected at the surface is dissipated in the interior. This dissipation thus inhibits the creation of a modal structure within the whole fluid column and the bottom presents the characteristics of radiative waves without rigid lid. In conclusion, lee waves observed in the simulation are thus qualitatively in accordance with the "radiating" linear theory near the bottom.

To quantitatively compare the simulation with the linear theory, the bottom values of different fields are shown in Fig. 10. As seen before, the intensity and shape of the vertical velocity matches with the theory. It shows the tendency of particles advected by the current to "climb" over the seamount upstream, and to go down the seamount downstream.

The lee waves-induced pressure is calculated from the simulation outputs. Firstly the density is computed from the salinity  $S$  and the temperature  $T$  with the TEOS-10 equation of state. A spatial high-pass filter is then applied on the time low-passed density. The filter is applied horizontally in the direction of the section at a cutting length  $\lambda_{\text{cut}} = 10 \text{ km}$ . This filter removes the density background which varies both horizontally and vertically and extracts an anomaly of density  $\rho'$ . Because the filter is applied on the time low-passed field, and  $\lambda_{\text{cut}}$  being chosen with respect to the along-section variations of topography,  $\rho'$  may be considered as the density anomaly due to lee waves. The CROCO model solving the hydrostatic primitive equations, the pressure anomaly is computed with

$$p'(z) = - \int_z^0 dz' \rho' g. \quad (29)$$

$z=0$  is the surface of the ocean where the pressure anomaly is known and equal to zero. The result of this calculation shown on Fig. 10 agrees with the theoretical prediction with a positive pressure anomaly upstream and a negative one downstream. Linear theory predicts that the pressure anomaly intensity depends on the cross-section elongation of the seamount [1]. The accordance between the simulation calculation and the theory is due to the fact that the theoretical code computes 3D theory instead of the classic 2D theory of textbooks.

This kind of internal wave extracts energy from the mean flow. In order to quantify it, the energetic balance of internal waves may be written as [1]:

$$U \partial_x \left( \underbrace{\frac{1}{2} \rho_0 |\mathbf{u}'|^2}_{(A)} + \underbrace{\frac{1}{2} \frac{g^2 \rho'^2}{\rho_0 N^2}}_{(B)} \right) + \nabla \underbrace{(p' \mathbf{u}')}_{(C)} = -\rho_0 U_z u' w' \quad (30)$$

where the part (A) is the kinetic energy density perturbation, the part (B) is the potential energy density perturbation and the part (C) is the energy flux perturbation in 3 dimensions. Considering a weak mean shear (i.e  $U_z \sim 0$ ), the wave energy is conserved, and the vertical energy flux generated by linear lee waves is thus  $F_{e^z} = p' w'$ . Because the troughs and crest of the perturbation pressure coincide with the vertical velocity, the vertical energy flux is found positive on the ground, as predicted by linear theory. It means that lee waves propagate energy upward.

Such energy flux has already been measured by EM-APEX profiling floats in the Drake passage [4]. The authors observed a large lee wave generated by the Antarctic Circumpolar Current (ACC) over a ridge about 1.5 km tall. They found a vertical energy flux of  $O(1) \text{ W.m}^{-2}$ . The ACC horizontal velocity at 100 m depth in the region is about  $0.5 \text{ m s}^{-1}$  while the Gulf Stream flows at about  $1 - 1.5 \text{ m s}^{-1}$ .

The Drake passage ridge being 30 times taller than the seamount studied in Fig. 10, and the velocity 3 times lower, a factor 10 can be assumed between the Drake passage case and the seamount case of the CROCO simulation. The peak value of  $F_e^z = O(0.1) \text{ W m}^{-2}$  in the simulation is thus in accordance with the Drake passage observations.

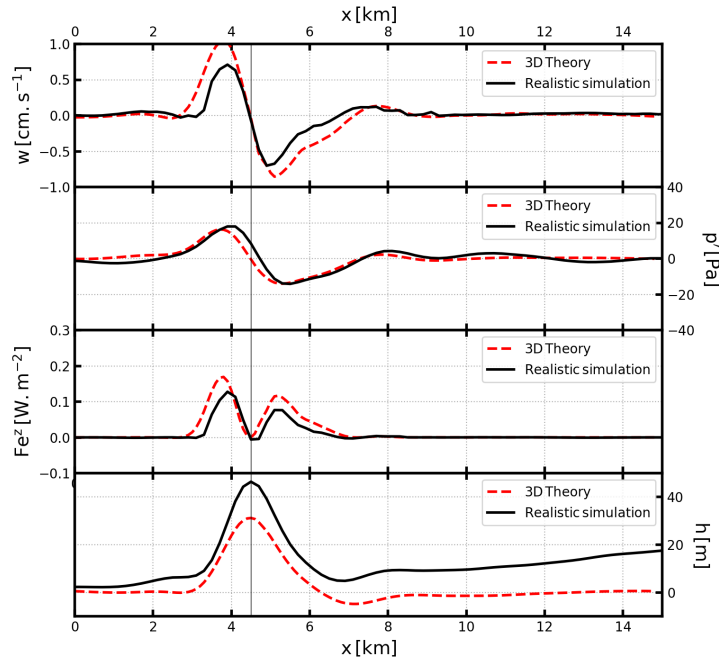


Figure 10: Comparison of the vertical velocity  $w$  at bottom (top), pressure anomaly  $p'$  at bottom (middle top), vertical energy flux  $F_e^z$  at bottom (middle bottom) and bathymetry  $h$  (bottom) between 3D hydrostatic theory (red dashed line) and CROCO simulation (black solid line).

### 4.3 Diagnostics over the bump

The lee waves generation agreeing with linear theory (at least at the bottom), this section focuses on analyzing what is happening over our main region of interest: the Charleston Bump. To do so, an along-flow section is chosen over the bump, called section 2 in Fig. 6, where a clear pattern of lee wave generation is seen in the horizontal cut of vertical velocity (Fig. 6). A snapshot of vertical velocity along this section is shown in Fig. 11(a).

The region over the bump has the characteristic of being very shallow ( $O(500)$  m) with a rough topography over which the Gulf Stream flows intensely. The section shows that these conditions generate a significant amount of lee waves, which can be seen over each seamount. In contrast with the case studied in the previous section, the vertical structure of the waves here is clearly modal because of the thickness of the fluid layer which is very close to  $2\pi U/N$ , the theoretical vertical wavelength of hydrostatic lee waves.

Contours of constant density (isopycnals) are also shown on Fig. 11. It shows that where the vertical velocity is positive (resp. negative), the horizontal along-current gradient is mostly positive (resp. negative). Because the density distribution and the vertical velocity are very correlated, lee

waves seems to generate an important vertical advection of fluid particles throughout the whole fluid layer. The height of the surface mixed layer  $h_{SML}$  is also computed. To do so, a typical variation of density  $\delta\rho$  is chosen, and we define

$$h_{SML} = |z(\rho_{surf}) - z(\rho = \rho_{surf} + \delta\rho)| \quad (31)$$

where  $\rho_{surf}$  is the density at the surface and  $\delta\rho = 50 \text{ g m}^{-3}$  (fixed arbitrarily). It isolates the layer where the density is quasi-homogeneous. The result shows a variation of the surface mixed layer clearly correlated with the variations of bathymetry. It indicates that the depth of the pycnocline is impacted by the lee waves generated on the ground. This conclusion may be important because the pycnocline is a place where a lot of biological process occur. Notably, it has been suggested that the variations in the vertical structure of the ocean (i.e. pycnocline and thermocline) could be one of the more important causes of variation in regional plankton diversity [10]. Internal waves such as lee waves therefore appear as an important mechanism in the evolution of biological processes.

Similarly, the height of the bottom mixed layer is computed using

$$h_{BML} = |z(\rho_{bot} - \delta\rho) - z(\rho_{bot})| \quad (32)$$

where  $\rho_{bot}$  is the density at the bottom. The result shows that this layer is about as large as the surface mixed layer. It also highlight the impact of lee waves on the shape of the bottom mixed layer, similarly than for the surface one.

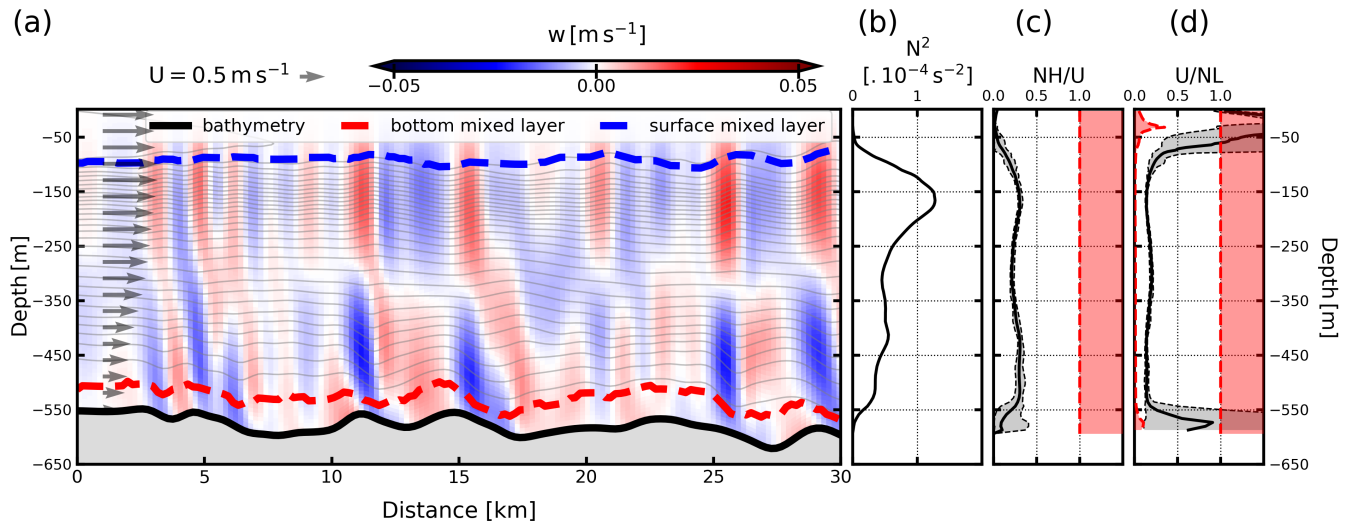


Figure 11: (a) Snapshot of time low-passed vertical velocity at location 2 (Fig. 6), gray contours indicate the isopycnals, arrows indicate the velocity profile (tangential to the section). (b),(c),(d) along-section averaged profile of stratification  $N^2$ , lee waves Froude Number  $NH/U$  and radiation parameter  $U/NL$  with max and min delimited area shaded in grey. In (b) the red area indicates the values of  $NH/U$  for which lee waves are predicted to be non-linear. In (c) the red area indicates the values of  $U/NL$  for which waves can not propagate (the left red dashed line indicates the profile of Prandtl number  $f/N$ ).

The Brunt-Väisälä frequency  $N$  is computed from the density (eq. (4)). It is averaged horizontally along the section. The result shows a maximum indicating the mean depth of the pycnocline at about 150 m (Fig. 11(b)).

To characterize the lee wave process, a lee-wave Froude number is calculated. The Froude number is a dimensionless number generally defined as the ratio of the advection by the flow to the wave propagation. In the case of lee waves, [11] shows by non-dimensionalizing the stratified Euler equations, that the correct Froude number is  $NH/U$ , where  $N$  and  $U$  are scales for the background stratification and velocity, and  $H$  is the scale of the bathymetry height. The authors thus show that this ratio corresponds to:

$$Fr_{\text{lee}} = \frac{NH}{U} = \frac{\text{vertical velocity within the lee wave}}{\text{group velocity of the lee wave}}. \quad (33)$$

[14] also discussed this parameter by calling it a "steepness" parameter. In these two papers, authors agree by stating that:

$$\begin{aligned} Fr_{\text{lee}} < 1 &\rightarrow \text{linear propagation of the waves} \\ Fr_{\text{lee}} \gtrsim 1 &\rightarrow \text{non-linearity of the waves.} \end{aligned} \quad (34)$$

In the simulation we compute typical height scale of the bathymetry  $H$  using a peak detection algorithm. Each seamount is defined by a local maximum and two minima (upstream and downstream). The difference between the maximum and the minimum is computed both upstream and downstream. Averaging the two quantities gives a mean height for each seamount. In the case of this section, one assumes that all seamounts have about the same height. Averaging the height of all seamounts gives here  $H = 37 \text{ m}$ .  $Fr_{\text{lee}}$  is then computed locally in the whole section and averaged along the section. It gives the lee-waves Froude number profile shown in Fig. 11(c). It highlights the fact that lee waves have a linear behavior.

In the case of lee waves, the condition for hydrostatic flow defined in (8) can be re-written in terms of an adimensionned number  $\varepsilon$  such that:

$$\varepsilon = \frac{U}{NL} \ll 1 \rightarrow \text{Hydrostatic} \quad (35)$$

where  $L$  is the typical scale for the length of seamounts (see Fig. 2). Using the same peak detection that before,  $L$  is defined as the distance between the lows of the bathymetry. Furthermore, relation (9) can be re-written in terms of  $\varepsilon$  such as :

$$Prdtl < \varepsilon < 1 \quad (36)$$

where  $Prdtl = f/N$  is the Prandtl number. As for the lee-wave Froude number,  $\varepsilon$  is computed locally and averaged along the section. The resulting profile is shown in Fig. 11(d). It shows that in the interior (1) the radiation condition is respected and (2) the hydrostatic condition is satisfied. This justifies the using a hydrostatic model for this study.

In conclusion, over the Charleston bump, linear lee waves are generated by little topographic seamounts of only  $O(< 50) \text{ m}$  tall. Such waves can then propagate in the fluid column upward to the surface mixed layer and impact the pycnocline depth. The small roughness of the ground induces large vertical velocities of  $O(1) \text{ cm s}^{-1}$  which may have a significant impact on vertical-motion-induced processes such as mixing. Furthermore the dynamic at the bottom seems to be more complex than just the lee wave process, and need further investigations. The study of such processes is the subject of the next section.

## 5 Dissipation, mixing and non-linear processes

### 5.1 Bottom mixed-layer depth from in-situ data

In the previous section, we have seen that the bottom mixed layer can be as thick as the surface mixed layer in some extreme region (like the Charleston Bump). Studies using in-situ data have already shown that the bottom mixed layer could be  $O(100)$  m thick over the Charleston Bump [20].

In order to compare this study with the simulation outputs, gliders data used in [20] have been uploaded from [21]. This data provide high-resolution transects across the Gulf Stream along the U.S. East Coast including some over our simulation domain (see trajectories on Fig. 12(b)). An example of such transects is shown in appendix C. Gliders were equipped with pumped Sea-Bird 41CP conductivity-temperature-depth (CTD) instrument. They thus provide profiles of temperature and salinity at a given horizontal position. For each profile, the thickness of the bottom is computed with (32). Gliders diving at maximum 1000 m depth, if the maximum depth of each profile did not correspond with the bathymetry at this position, the profile were removed (using bathymetry from the CROCO simulation). An average of the height of the bottom mixed layer is then computed in  $0.5^\circ \times 0.5^\circ$  boxes within the simulation domain (Fig. 12(a)). This average is in time and space because gliders data haven't been collected at the same time and at the same location. The results shows a bottom mixed layer of  $O(100)$  m over the region of the bump, and along the continental shelf. The computation of the standard deviation in the same boxes (Fig. 12(b)) gives an estimation of the variation of the bottom layer in time and in space. This variation is very important over the bump. This is due to the fact that (1) this region presents a time variation of the current when the Charleston Gyre moves Northward and Southward along the shelf and (2) the bottom current is maximum in this region. This intensification may generate a lot of non-stationary or/and non-linear processes which are probable causes of the bottom mixed layer expansion.

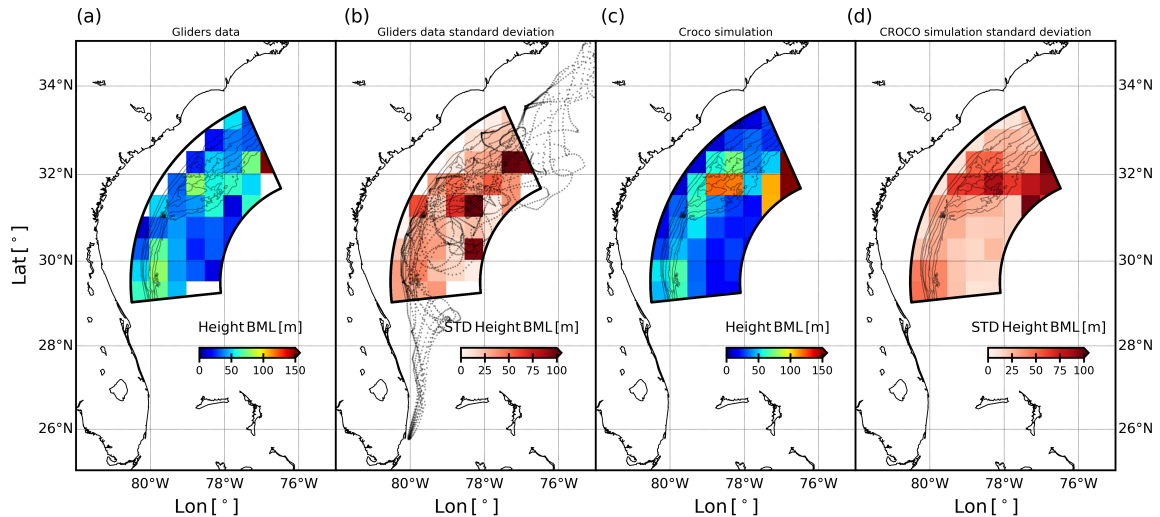


Figure 12: Bottom mixed layer thickness calculation in  $0.5^\circ \times 0.5^\circ$  boxes. (a) Mean thickness from gliders data. (b) Standard deviation of thickness from gliders data, grey dots indicate the trajectories of gliders. (c) Mean thickness from simulation. (d) Standard deviation of thickness from simulation. On each map, gray contours indicate bathymetry levels between 0 and 800 m every 100 m.

The mean height of the bottom mixed layer and its (time and spatial) standard deviation are also computed from the simulation (Fig. 12(c) and Fig. 12(d)). The results shows also a quite thick

bottom mixed layer of  $O(100 - 150)$  m over the bump and along the shelf. Despite the fact that the height is more important in the simulation, the regions where the bottom layer is thick are quite the same that in gliders observations. Furthermore, a net correlation can be made between the standard deviation from simulation and from observation: there is a lot of variation along the shelf and over the bump. In this regions, the important thickness of the bottom mixed-layer may be due to vertical mixing (through non-linear processes) and some energy dissipation may occur in this region.

## 5.2 Quantification of the dissipation and energy budget

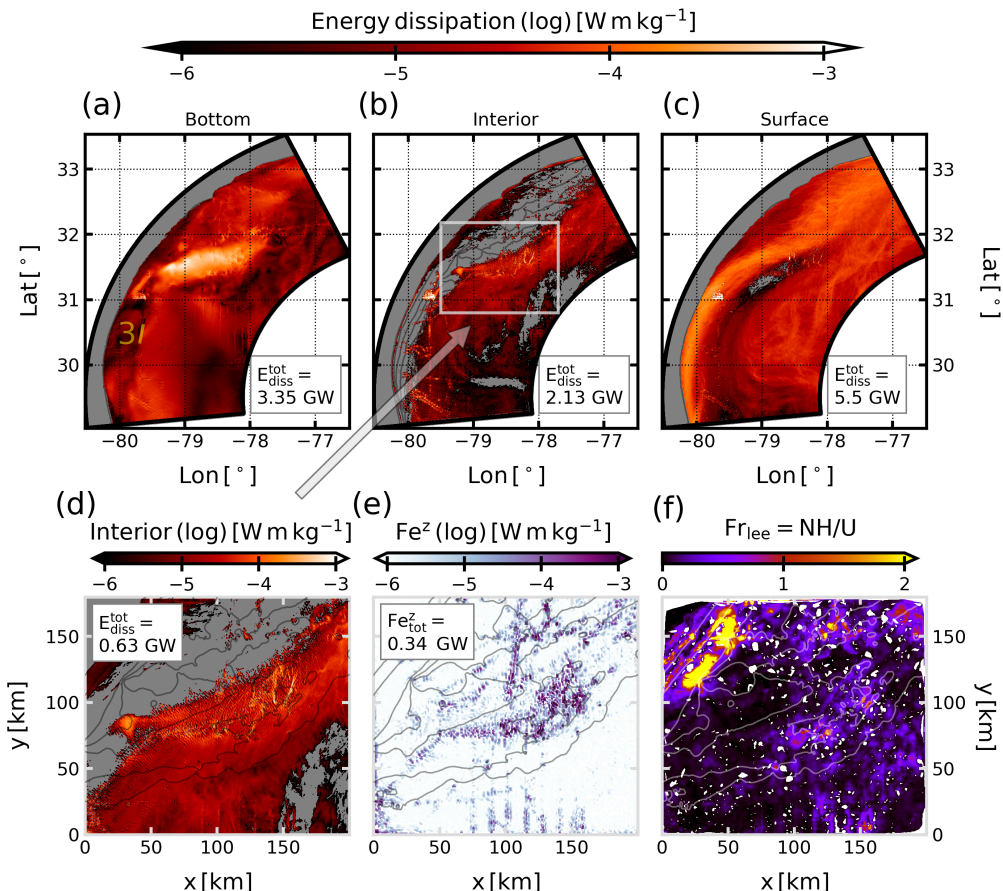


Figure 13: Energy dissipation due to vertical mixing. (a), (b) and (c) Energy dissipation from vertical mixing at the bottom, in the interior and at the surface. (d), (e) and (f) Focus on the area delimited by the grey rectangle in (b). (d) Dissipation in the interior. (e) Vertical energy flux of lee waves  $Fe^z$  at the bottom. (f) Lee-wave Froude number. All quantities are time-averaged over the whole simulation. The contours indicate bathymetry levels between 0 and 800 m every 200 m. The grey-shaded areas represent regions where either the energy dissipation is positive or the whole fluid column is mixed (i.e. no surface or bottom mixed layer can be defined).

To quantify the impact of lee waves and nonlinearities, the kinetic energy budget is analyzed. The kinetic energy equation can be calculated by taking the inner product of the horizontal velocity with

the Navier-Stokes equations. It gives:

$$\frac{1}{2}\partial_t u_i^2 + \frac{1}{2}u\partial_x u_i^2 + \frac{1}{2}v\partial_y u_i^2 + \frac{1}{2}w\partial_z u_i^2 = -\frac{u_i}{\rho_0}\partial_{x_i} P + \mathcal{V}u_i + \mathcal{D}u_i + \mathcal{S}u_i \quad (37)$$

for the two components of the velocity (i.e  $i = 1, 2$ ), where  $\mathcal{V}$  is the vertical mixing ( $\mathcal{V} = \partial_z(K\partial_z \mathbf{u})$ ),  $\mathcal{D}$  is the horizontal diffusion, and  $\mathcal{S}$  other sources and sinks. Each term of (37) is computed 'online' by the model. In the following we focus on the quantity:

$$E_{\text{diss}} = \mathcal{V}u + \mathcal{D}u + \mathcal{V}v + \mathcal{D}v \quad (38)$$

which represents the vertical mixing and horizontal diffusion part of the energy budget. Because horizontal diffusion is weak, we assume that  $E_{\text{rhs}}$  represents the energy dissipated by the vertical mixing in the simulation. The numerical model has implicit horizontal dissipation through its advection scheme, and vertical dissipation based on parameterizations of the vertical mixing (for more details see [8]).

The energy dissipation at the bottom (Fig. 13(a)), and at the surface (Fig. 13(c)) are calculated by integrating  $E_{\text{RHS}}$  respectively in the bottom mixed layer and in the surface mixed layer. The energy dissipation in the interior (Fig. 13(b)) is also computed by integrating  $E_{\text{RHS}}$  in the layer between the bottom and the surface layers.

In Fig. 13(a), (b) and (c) the total dissipated energies over the domain are shown in inserts (calculated by integrating horizontally the energy dissipation). In addition, the time evolution of such dissipated energies over the bump is shown in appendix D. It shows that the dissipation by vertical mixing is dominant in the surface layer. The map of surface dissipation also highlights the fact that this dissipation is important along the shelf, where the Gulf Stream is the strongest.

Despite this, a non-negligible amount of energy is dissipated in the interior. In particular, the map shows a pattern of dissipation at the eastern edge of the Charleston Bump. This pattern is localized where intense lee-waves are observed in the simulation (see Fig. 6(c)). A zoom in a region over the Charleston Bump is shown in fig 13(d). In this specific region  $O(0.5)$  GW is dissipated in the interior.

To quantify the contribution of lee waves in such dissipation, the vertical energy flux generated by lee waves  $F_{\text{e}}^z = p'w'$  at the bottom is computed. The calculation is made with time low-passed simulation outputs. To compute the pressure anomaly, a spatial trend of the density is computed with a cubic smoothing spline with a fall-off chosen to keep only the small scales contribution. The pressure is then computed with (23). The result of this calculation in the region over the bump is shown in Fig. 13(e). It highlights an area where a lot of lee waves are generated. This region is the same that the one where dissipation is observed in the interior. Furthermore, by summing this energy flux horizontally gives a flux of energy  $O(0.5)$  GW. This order of magnitude is similar to that of the dissipation in the interior. It allows us to conclude that the impact of lee wave in the dissipation in this region is non negligible.

The energy flux discussed earlier is computed assuming linear lee waves, whereas dissipation occurs when non-linear process are involved. To discuss of the non-linearity of lee waves in the region, the lee wave Froude number  $NH/U$  is computed. To do so, a peak detection is performed on the de-trended topography in directions  $x$  and  $y$ . For the computation over  $x$  for instance, the peak detection discussed in section 4.3 is used for each  $y$ -position along the  $x$ -axis. It gives a map of the height of the seamounts in the region. This map is then interpolated on a regular grid. The result in direction  $x$  and  $y$  are then averaged giving a map of  $H$ . The Froude is finally calculated by taking a mean value of  $N$  and  $U$  near the bottom. Since we have seen earlier that the Froude does not vary vertically (see Fig. 11(c)), this calculation is representative of the horizontal distribution of the Froude number over the Charleston bump. The result is shown in Fig. 13(f). It highlights the fact that  $Fr_{\text{lee}}$  is close to the unity at the

eastern edge of the bump, where we have observed an important energy dissipation in the interior. In the interior, one of the few process occurring is internal waves such as lee waves. The dissipation in the interior may thus be due to the vertical mixing induced by the breaking of lee waves becoming non-linear.

[13] showed that approximately 0.2 TW is converted into lee waves in the global ocean and that about half of this energy is dissipated. Here one can assume that O(1) GW of energy is dissipated in the interior because of lee waves in the whole simulation domain. In this region around the Charleston Bump, the nonlinearities of lee waves in the interior are thus responsible for about 1% of the dissipated energy by lee waves in the global ocean.

However, the dissipation in the interior is much lower than the dissipation at the bottom. The bottom dissipation varies a lot during the month of the simulation (see appendix D). Time variations and horizontal distribution of the bottom current being correlated with intensification of the mean current, the bottom dissipation is principally driven by the near bottom flow over the (rough) topography. The vertical mixing at the bottom may occur because of plenty of turbulent boundary layer processes. To understand what is happening at the bottom, the next section focuses on the section 3 indicated in Fig. 6 and Fig. 13(a).

### 5.3 Focus on local dissipation

The region discussed in this section is interesting because even though it is quite isolated, bottom and interior energy dissipation are important (Fig. 13(a) and (b)) and some non-linear processes happen during the simulation. The section is chosen tangential to the mean current. A seamount which forces the generation of lee waves is present in the middle of the section.

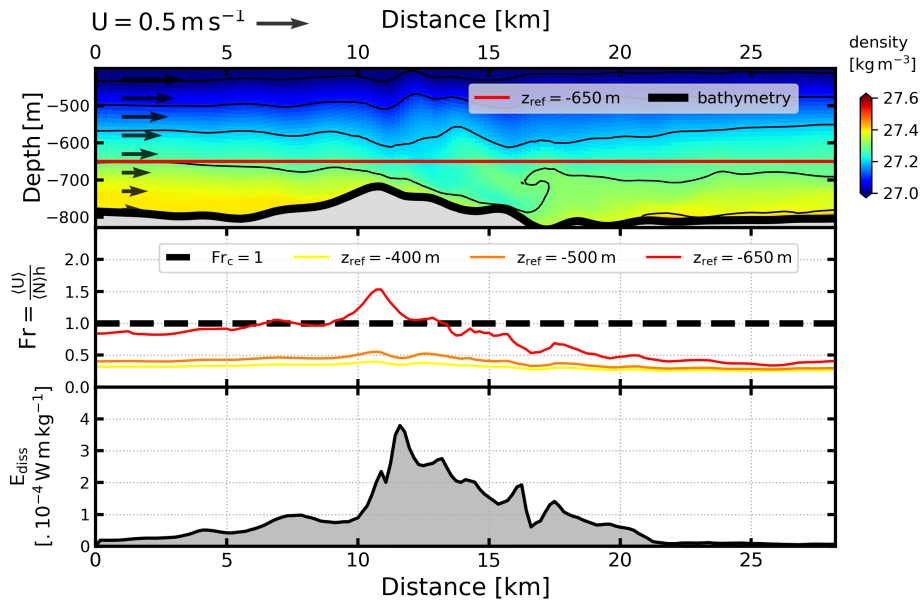


Figure 14: Section illustrating the vertical mixing process. (top) Snapshot of density at location 3 (Fig. 6) on April 5th, black contours indicate the isopycnals, arrows indicates the velocity profile (tangential to the section). (middle) Hydraulic-jump Froude number computed with depth averaged velocity  $U$  and stratification  $N$  from bottom to  $z_{\text{ref}}$ , for different values of  $z_{\text{ref}}$ . (bottom) Depth integrated (from bottom to  $z_{\text{ref}} = -650 \text{ m}$ ) dissipation of energy. The dissipation is time-averaged over the "hydraulic jump episode".

The time evolution of what is happening at the bottom of the section is presented in appendix E. At the beginning of the simulation, the near bottom current is weak. The current then increases and internal waves are generated above the seamount. On April 5th, a so-called 'hydraulic jump episode' occurs. This event is shown in Fig. 14. The density distribution at the bottom shows a region (at about  $(x, z) \sim (16 \text{ km}, -700 \text{ m})$ ) where the isopycnal  $\rho = 27.3 \text{ kg m}^{-3}$  looks like a breaking wave. At this location some heavy water passes over some lighter one and some mixing may occur.

The shape of the streamlines here is very similar to a phenomena often discuss in hydrodynamics literature: *hydraulic jumps*. In a stratified flow, the distinction between a breaking lee wave and an hydraulic jump is not clear. The difference is principally semantic. In the case of lee waves one talks about the breaking of the wave, while in the case of hydraulic jump one talks about the transition between a subcritical and a supercritical flow.

To discuss in terms of critical flows in our case, a 'hydraulic jump Froude number'  $\text{Fr}$  is computed. As for the lee wave case, the choice of a correct Froude to describe the flow is not straightforward. For a stratified flow in an open canal, the literature (for instance [19]) usually defines the Froude such as

$$\text{Fr} = \frac{U}{Nh} \quad (39)$$

where  $h$  is the height of the water column (i.e. the total depth). It corresponds to the ratio of the velocity of the flow to the velocity of the first mode of gravity waves. Depending on the value of this number, it says that:

$$\begin{aligned} \text{Fr} < \text{Fr}_c &\rightarrow \text{subcritical flow} \\ \text{Fr} \gtrsim \text{Fr}_c &\rightarrow \text{supercritical flow} \end{aligned} \quad (40)$$

with  $\text{Fr}_c = 1$  is the critical Froude number. If the flow is supercritical upstream and subcritical downstream a specific location, a stationary hydraulic jump is formed at this location and some energy is dissipated by the jump. In the literature, the hydraulic jump is occurring in a layer of height  $h$  where  $U$  and  $N$  are assumed constant. In the case observed in the simulation, the event is localized at the bottom of the fluid.  $h$  is thus defined as the height between the ground and a typical level  $z_{\text{ref}}$ , describing the 'bottom active layer', where the hydraulic jump is occurring. The velocity of the fluid and the stratification are averaged in this layer, giving depth averaged  $\langle U \rangle$  and  $\langle N \rangle$ . It gives an horizontally-varying Froude number describing the hydraulic jump event. The result is shown in Fig. 14 (middle) for different values of  $z_{\text{ref}}$ . Choosing  $z_{\text{ref}} = -650 \text{ m}$ , gives a good characterization of the hydraulic jump observed and motivate the choice of such bottom layer. The flow is supercritical at the top of the seamount since  $\text{Fr} > 1$  and subcritical in the lee of the seamount. (Time evolution of the Froude number shows that it exceeds 1 only when the jump occurs.)

Hydraulic jumps are the place where energy is dissipated. To quantify this dissipation, the energy dissipation by vertical mixing  $E_{\text{diss}}$  (definition (38)) is integrated in the layer used for the computation of the Froude number (i.e. between  $z_{\text{ref}} = -650 \text{ m}$  and the ground). This value is also time averaged over the hydraulic jump episode (about 2 days long). The result is shown in Fig. 14(bottom). It shows that a significant amount of energy is dissipated above the seamount. The order of magnitude of this dissipation ( $O(10^{-4}) \text{ W m kg}^{-1}$ ) is close to the one observed in some regions over the Charleston Bump in the bottom mixed layer and at the surface (see Fig. 13). It allows us to conclude that an important part of the energy dissipated by vertical mixing in the simulation may be due to that kind of hydraulic jump effect.

In conclusion, an important amount of energy is dissipated at the bottom by vertical mixing. This mixing is mostly due to the shearing and frictional effects where the bottom current is strong. Locally we have seen that this dissipation may be due to the breaking of lee waves (also called hydraulic jump).

A non-negligible part of the energy is also dissipated by lee waves in the interior of the ocean, where such waves are subject to nonlinearities and where the vertical energy flux of lee waves is important.

## 6 Conclusion

During this internship, I have studied the generation of internal lee waves in the Gulf Stream path using both theory and a realistic simulation.

We do observe in our simulation the generation of lee waves that are in qualitative agreement with previous observations from satellite and sea-gliders observations. Secondly, we highlighted the fact that in the simulation the shape of the waves agrees with the linear theory at the bottom of the ocean. Linear theory is able to reproduce the essential properties of observed lee waves, at least as far as their generation and amplitude are concerned. Furthermore, we have shown that these waves are essentially in hydrostatic and linear regime according to typical dimensionless numbers (e.g. lee wave Froude number). We have observed that a significant amount of energy ( $O(1)$  GW) is being dissipated in the interior of the fluid. This dissipation takes place where some energy is radiated upward by lee waves, and where these waves are subject to nonlinearities. Finally, the study of the breaking of lee wave has shown that such phenomenon creates an important dissipation ( $O(10^{-4})$  W m kg $^{-1}$ ) near the bottom. This order of magnitude is comparable for instance with the dissipation induced by centrifugal instability [7] in the ocean. This kind of phenomenon have thus to be taken into account in the global lee-wave dissipation budget.

Through vertical mixing, lee waves provide a mechanism for the transfer of energy from large-scale flows to turbulent length scales. In particular over the Charleston Bump, this mechanism is substantial since it represents approximately 1% of the dissipated predicted by [13] in the whole ocean by the breaking of lee waves.

To go further, a finest study of this near-bottom phenomenon could be done, especially by separating the model-parameterized drag from the breaking of lee waves. This may allow to quantify the lee-wave-induced dissipation at the bottom. A study of the lee-wave-induced mixing could also be done by studying the potential energy variations in the interior. Finally, adding a rigid lid condition in the theoretical calculation could allow to compare the theory with the waves in the simulation where the layer is shallow.

## A Basic theory for the ocean dynamics

This section aims at presenting some definitions which are used in this report. It sets the main equations that underlie the physical oceanography.

### A.1 From momentum equations to primitive equations

Start from Navier-Stokes equations for a fluid of density  $\rho$  in a rotating frame of reference :

$$\frac{d}{dt} \mathbf{u} + 2\boldsymbol{\Omega} \times \mathbf{u} = -\frac{1}{\rho} \nabla P - g \cdot \mathbf{e}_z + \mathbf{F} + \mathbf{D} \quad (41)$$

Projecting the rotation vector of earth over a local frame gives

$$2\boldsymbol{\Omega} \times \mathbf{u} = \begin{pmatrix} -fv + f^*w \\ fu \\ -f^*u \end{pmatrix} \quad (42)$$

where  $f = 2\Omega \sin\phi$  and  $f^* = 2\Omega \cos\phi$  are the "traditional" and "non traditional" Coriolis parameters ( $\phi$  is the latitude). Far from the equator (where  $\phi \sim 0$ ) the non-traditional component of the Coriolis parameter can be neglected. Making this assumption and the Boussinesq approximation, one obtain a set of equation called *Primitive equations* :

$$\frac{d}{dt} \mathbf{u} + f \mathbf{e}_z \times \mathbf{u} = -\frac{1}{\rho_0} \nabla P - \frac{\rho'}{\rho_0} g \cdot \mathbf{e}_z + \mathbf{F} + \mathbf{D} \quad (43)$$

### A.2 Density evolution and Brunt-Väisälä frequency

The distribution of salinity S and temperature T impact the distribution of density in the water column. An equation describing the evolution of density can be written. Starting from mass conservation

$$\frac{d}{dt} \rho + \rho \nabla \cdot \mathbf{u} = 0, \quad (44)$$

by assuming incompressibility  $\nabla \cdot \mathbf{u} = 0$  and the density decomposition (2) one can write

$$\frac{d}{dt} \rho' + w \partial_z \bar{\rho} = 0. \quad (45)$$

Dividing this equation by  $-g/\rho_0$ , the equation for the evolution of the density is:

$$-\frac{g}{\rho_0} \frac{d}{dt} \rho' + w N^2 = 0. \quad (46)$$

## B WKBJ approximation

The solution of (15) can be found using the WKBJ approximation. Physically, we consider the trajectories of wave packets of wave energy for given wave number, where this wavenumber is determined locally by N and U. This method of resolution is called after Wentzel, Kramers and Brillouin who developped this method to find an approximate solution of the wave equation. This method is notably used to solve the time-dependent Schrödinger equation. Mathematically, we set that

$$\tilde{\eta} = A(\varepsilon z) e^{i \frac{\theta(\varepsilon z)}{\varepsilon}} + O(\varepsilon^2).$$

with  $\varepsilon \ll 1$ . Injecting this form of solution into (15) gives:

$$\begin{aligned} n^2 &= (\partial_z \theta)^2 && \text{at } O(\varepsilon^0) \\ 2(\partial_z A)(\partial_z \theta) + A(\partial_z^2 \theta) &= 0 && \text{at } O(\varepsilon^1) \end{aligned}$$

which finally gives:

$$\begin{aligned} \theta &= \int_0^z dz n(z) \\ A(z) &= A(z = 0) \sqrt{\frac{n(z = 0)}{n(z)}} \end{aligned}$$

and the form of the displacement of a streamline given by (22).

## C Transect from gliders

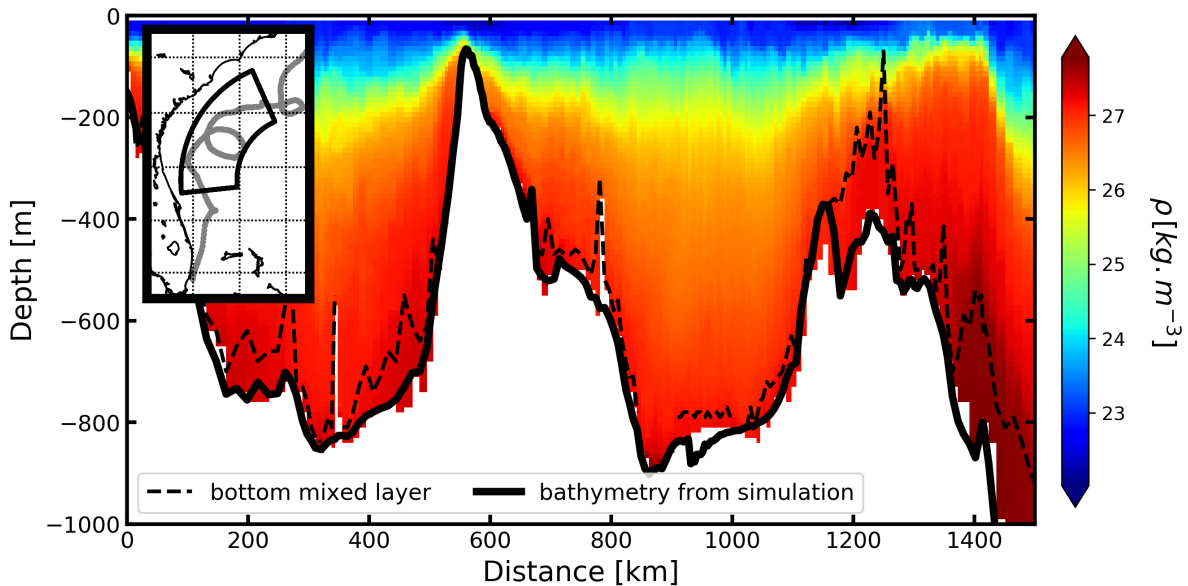


Figure 15: Density measurement from a glider mission, insert presents the trajectory of the glider during the mission. Black dashed line presents the position of top of the bottom mixed layer computed with (32) and black solid line presents the bathymetry from the simulation.

## D Time evolution of dissipation

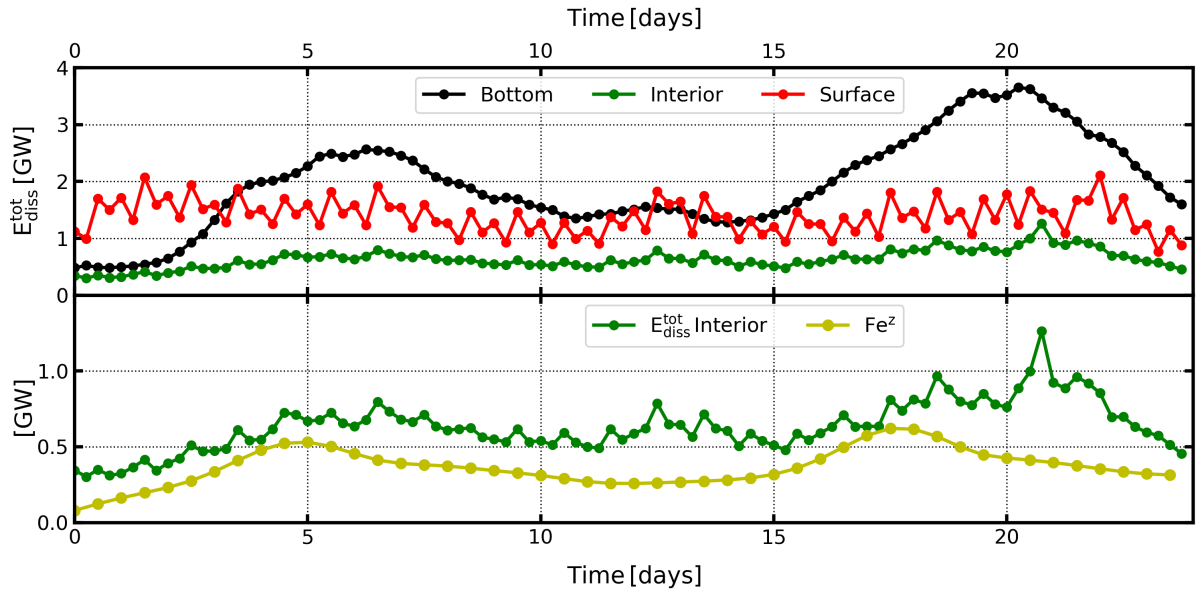


Figure 16: Time evolution of horizontal summed dissipation over the Charleston Bump (area delimited by the grey rectangle in fig13(b)). (top) Comparison between the dissipation at the bottom, in the interior and at the surface. (bottom) Comparison between the dissipation in the interior and the vertical energy flux of lee waves.

The time evolution shows a quasi-periodic evolution of the dissipation at the surface with a period of  $\sim 1$  day. This periodicity is due to the diurnal variability of the surface mixed layer depth (implemented by a specific function in the model). It highlights the fact that there is much mixing during the night. Indeed, water at the contact of the atmosphere cools down and sinks in the interior. It results in an intense mixing at the base of the surface layer and an increasing of the height of the surface layer during the night. The dissipated energy in the surface layer is thus bigger at night.

## E Hydraulic jump event

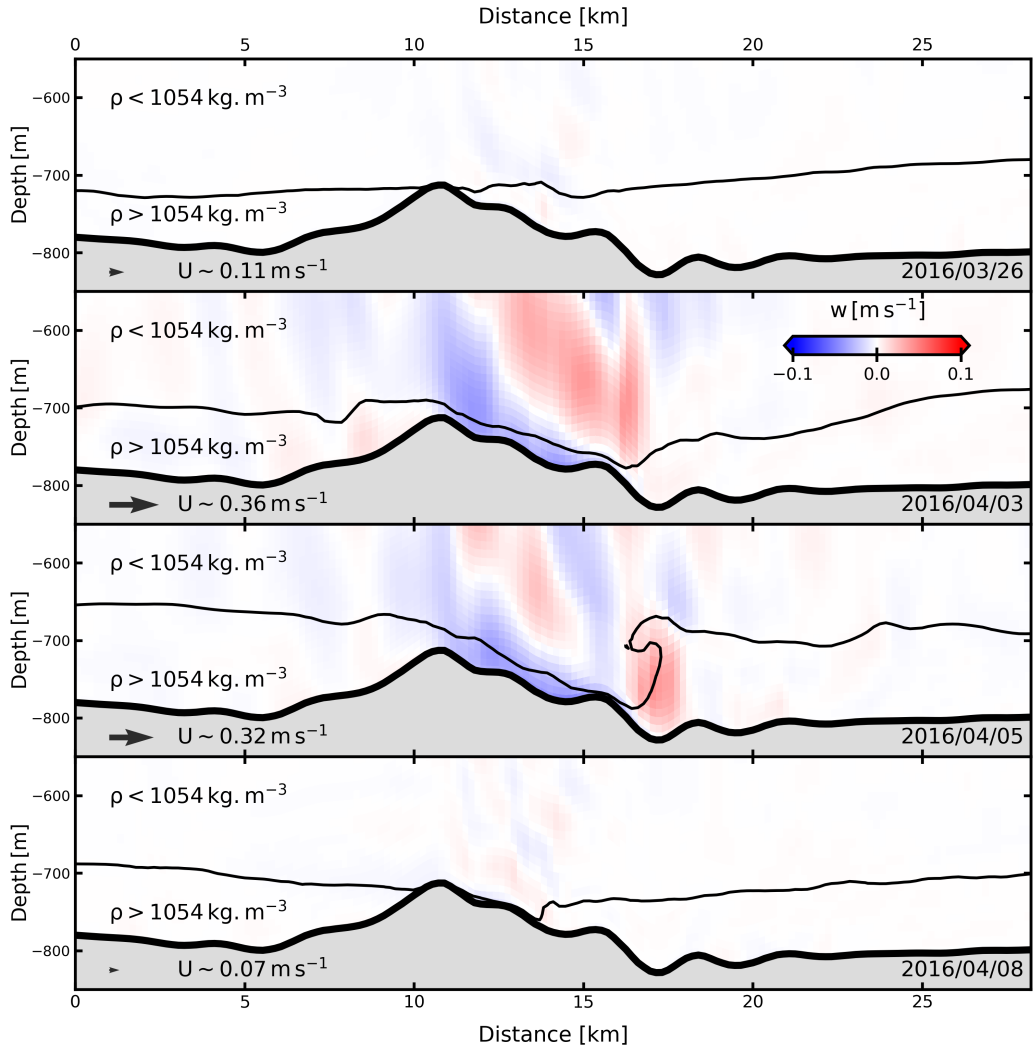


Figure 17: Hydraulic jump episode. On March 26th the near bottom current is weak and no waves is generated. On April 3rd the current becomes intense the streamline is deformed as predicted by the linear theory. On April 5th the wave downstream breaks, the shape of the streamline is typical of an hydraulic jump episode. On April 8th the current is weak and and wave propagation vanishes

## F Energy conversion into lee waves

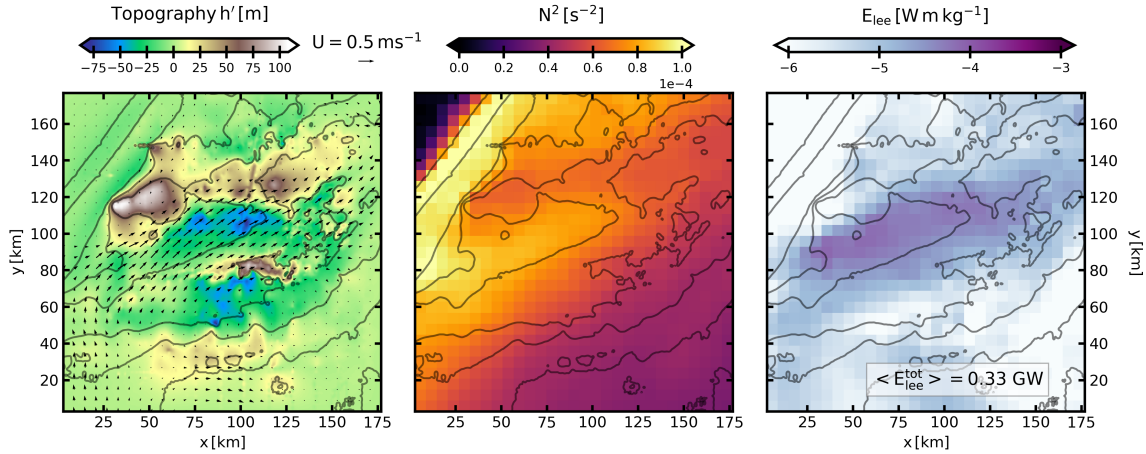


Figure 18: Energy conversion into lee waves according to linear theory. (left) Topography anomaly  $h'$  obtained by de-trending the topography and near-bottom current used for the calculation of the energy. (middle) Brunt Väisälä frequency  $N^2$  used for the calculation of the energy. (right) Energy flux converted into lee waves, the insert indicates the energy flux integrated over the whole domain. Each field is time-averaged over the simulation. For each map, black contours indicate bathymetry levels from 0 to 800 m every 200 m.

To compute the energy converted into lee waves with observations, we have to know the value of the vertical velocity near the bottom of the ocean (see (30)). Compute such flux within a large area is, in practice, impossible. To make an estimation of the flux, an other approach is possible using the linear theory.

The form drag exerted by the topography on the mean flow is

$$F(x, y) = p'(x, y, z = 0) \nabla h(x, y).$$

(This drag is equal to the vertical momentum flux of lee waves [6] such that

$$F(x, y) = \rho_0((u'w')^2 + (v'w')^2)^{1/2}.)$$

By passing into Fourier space, and using the fact that the wave drag is linked to the energy flux through the wave action, [2] shows that the energy converted into lee waves is:

$$E_{\text{lee}} = \frac{\rho_0}{4\pi^2} \iint_{-\infty}^{+\infty} P_h(k, l) \frac{(\mathbf{U} \cdot \mathbf{k})}{|\mathbf{k}|} \sqrt{N^2 - (\mathbf{U} \cdot \mathbf{k})^2} \sqrt{(\mathbf{U} \cdot \mathbf{k})^2 - f^2} dk dl \quad (47)$$

where the velocity  $\mathbf{U}$  and the stratification  $N$  have to be estimated at the bottom, and  $P_h$  is the power spectrum of the topography. This expression is valid for small topographies.

[13] and [14] typically use this expression in order to estimate the energy converted into lee waves. Particularly, [13] shows that 20% of the global wind power input into the ocean is converted into lee waves (about 0.2 TW). The authors also highlight that in extreme region such as the ACC region, the energy flux is  $O(10 - 100) \text{ mW m}^{-2}$ .

To compare these results with our simulation, the calculation of the energy flux is computed using equation (47). The region of the calculation is the same that the one indicated in Fig. 13 by the grey

rectangle. The topography is de-trended to compute the power spectrum  $P_h$ . The velocity and the stratification are averaged in boxes ( $6 \times 6$  km) to reduce the calculation time, and averaged in the last 100 to avoid problems in the bottom mixed layer. The calculation is made every 12 hours and then averaged over the whole simulation.

The topography, mean velocity and mean stratification used for the calculation are shown in Fig. 18(left) and (middle). The energy converted into lee waves is shown in Fig. 18(right). It shows a maximum energy flux of  $83 \text{ mW m}^{-2}$  where the current is maximal. This value agrees with the estimation of [13]. Furthermore, the horizontally-integrated value of the energy is  $0.33 \text{ GW}$  which matches with the energy presented in Fig. 13(e). This calculation highlights the fact that the Charleston Bump is as important as extreme region such as the ACC region in terms of lee waves production.

## References

- [1] Peter G. Baines. *Topographic effects in stratified flows*. Cambridge University Press, 1995.
- [2] T.H. Bell. Topographically generated internal waves in the open ocean. *Journal of Geophysical Research*, 80:320–327, 1975.
- [3] J. Callies, R. Ferrari, J.M. Klymak, and J. Gula. Seasonality in submesoscale turbulence. *Nature Communication*, 6:6862, 2015.
- [4] J.M. Cusack, A.C. Naveira Garabato, D.A. Smeed, and J.B. Girton. Observation of a large lee wave in the drake passage. *Journal of Physical Oceanography*, 10:793–811, 2017.
- [5] R? Ferrari and C. Wunsch. Ocean circulation kinetic energy: reservoirs, sources and sinks. *Annual review of fluid mechanics*, 41:253–282, 2009.
- [6] Adrian E. Gill. *Atmosphere-Ocean Dynamics*. Academic press, 1982.
- [7] J. Gula, J.C. McWilliams, and J. Molemaker. Topographic generation of submesoscale centrifugal instability and energy dissipation. *Nature Communications*, 7:12811, 2016.
- [8] J. Gula, J. Molemaker, and J.C. McWilliams. Gulf stream dynamics along the southeastern u.s seabord. *Journal of physical oceanography*, 45:690–715, 2015.
- [9] J.C. Haney. Internal waves as sources of small-scale patchiness in seabird distribution on the blake plateau. *The American Ornithologists' Union*, 104:129–133, 1987.
- [10] A.R. Longhurst. Relationship between diversity and the vertical structure of the ocean. *Deep-sea Research*, 32:1535–1570, 1985.
- [11] F.T. Mayer and O.B. Fringer. An unambiguous definition of the froude number for lee waves in the deep ocean. *Journal of Fluid Mechanics*, 831:R3–1, 2017.
- [12] C. McClains and L. Atkinson. A note on the charleston gyre. *Journal of geophysical research*, 90:11 857–11 861, 1985.
- [13] M. Nikurashin and R. Ferrari. Global energy conversion rate from geostrophic flows into internal lee waves in the deep ocean. *American Geophysical Union*, 38:L08610, 2011.
- [14] M. Nikurashin, R. Ferrari, N. Grisouard, and K. Polzin. The impact of finite-amplitude bottom topography on internal wave genration in the southern ocean. *Journal of Physical Oceanography*, 44:2938–2950, 2014.
- [15] J. Nycander. Generation of internal waves in the deep ocean by tides. *Journal of Geophysical Research*, 110:C10028, 2005.
- [16] N. Raschle, B. Chapron, A. Ponte, F. Arduuin, and P. Klein. Surface roughness imaging of currents shows divergence and strain in the wind direction. *Journal of Physical Oceanography*, 44:2153–2163, 2014.
- [17] A. Shchepetkin and J.C. McWilliams. The regional oceanic modeling system: A split-explicit, free-surface, topography-following-coordinate ocean model. *Ocean Modelling*, 9:347–404, 2005.
- [18] A. Shchepetkin and J.C. McWilliams. Accurate boussinesq modeling with a practical, "stiffened" equation of state. *Ocean Modelling*, 38:41–70, 2011.
- [19] S.A. Thorpe. Turbulent hydraulic jumps in a stratified shear flow. *Journal of Fluid Mechanics*, 654:305–350, 2010.
- [20] R.E. Todd. High-frequency internal waves and thick bottom mixed layers observed by gliders in the gulf stream. *Geophysical Research Letters*, 44:6316–6325, 2017.
- [21] R.E. Todd and B. Owens. Gliders in the gulf stream (data set), 2016. Scripps Institution of Oceanography, Instrument Development Group.
- [22] Geoffrey K. Vallis. *Atmospheric and Oceanic Fluid Dynamics*. Cambridge University Press, 2017.
- [23] C. Wunsch. The work done by the wind on the oceanic general circulation. *Journal of Physical Oceanography*, 28:2331–2339, 1998.
- [24] Q. Zheng, B. Holt, X. Li, X. Liu, Q. Zhao, and Y. Yuan. Deep-water seamount wakes on seasat sar image in the gulf stream region. *Geophysical Research Letters*, 39:L16604, 2012.